Nonlinear Dyn (2023) 111:6533–6556
https://doi.org/10.1007/s11071-022-08162-3

ORIGINAL PAPER

Geometrical nonlinearities in a curved cantilever beam: a condensation model and inertia-induced nonlinear features

Xiang Sun · Gaetan Kerschen · Li Cheng

Received: 27 June 2022 / Accepted: 1 December 2022 / Published online: 23 December 2022

Abstract Subjected to high level forcing, flexible and curved beams exhibit pronounced geometrical nonlinearities. In particular, intrinsic nonlinearities of cantilevers are different from their counterparts with end-constrained boundaries and the combination of the enhanced nonlinear-inertia effects with initial curvature creates harsh demand on the modeling, numerical simulation and understanding of associated physical phenomena. This paper investigates the salient nonlinear features in a curved cantilever beam, with particular attention paid to the inertia-induced effects through both linear and nonlinear analyses. An inextensible condensation model, with the consideration of the initial curvature, is proposed based on a geometrically exact model for an Euler–Bernoulli cantilever beam. The free boundary of the cantilever gives rise to more significant longitudinal motion, which increases the inertia effects in the beam vibration which is in turn enhanced by the initial curvature. Specific techniques are proposed to numerically implement the developed model with increased accuracy and robustness. Numerical simulations are then conducted to validate the proposed model through comparisons with the finite element method, examine the assumptions underpinning the model and explore the salient physical features, in particular the inertia-induced effects in both linear and nonlinear cases. Results show a decrease in the natural frequencies due to the initial curvature effect, a transition of the first mode from hardening to softening caused by enhanced curvature-induced inertia effect, and a pronounced asymmetry of the higher order modes with respect to frequencies.

Keywords Geometrical nonlinearities · Curved cantilever beam · Inextensible model · Nonlinear inertia

1 Introduction

The wide use of lightweight and flexible structures in engineering applications has aroused persistent interest in studying their intrinsic nonlinear behaviors. Among various types of basic structural elements, beam-like structures with initial curvature are of particular interest to the scientific community, exemplified by rotor blades [1], buckled beams [2], thin-walled composite beams [3], imperfect micro-beams [4] and shallow arches [5, 6], etc. Their highly flexible

X. Sun · L. Cheng (✉)
Department of Mechanical Engineering, The Hong Kong Polytechnic University, Hung Hom, Kowloon, Hong Kong SAR, People's Republic of China
e-mail: li.cheng@polyu.edu.hk

G. Kerschen
Department of Aerospace and Mechanical Engineering, University of Liège, Allée de la Découverte 9, 4000 Liège, Belgium

and thin-walled nature usually results in large amplitude vibration which gives rise to significant geometrical nonlinearity and leads to rich and complex nonlinear dynamic behaviors which are absent in linear systems. Different from other types of nonlinearities such as mechanical or contact nonlinearity, geometrical nonlinearity is distributed over the entire structure, which makes the problem more complicated. While the literature provides rather comprehensive knowledge on the source of intrinsic nonlinearities as well as the resultant dynamic behaviors such as hardening/softening phenomena [7], existing condensation models are mostly associated with specific boundary condition [8, 9]. The so-called condensation model couples multi-dimensional internal forces or displacements to form one governing equation with explicit nonlinear terms. Moreover, the consideration of the initial curvature creates additional challenges in both system modeling, numerical implementation and the understanding of nonlinear phenomena with increasing complexities, such as the hardening-to-softening transition of the first mode in a shallow arch [6].

The issue has been predominantly addressed on clamped–clamped beams with initial curvature [3, 5, 6, 10]. The nonlinear stretching is an intrinsic nonlinearity feature specific to a clamped–clamped beam due to constrained ends. Among several contributions, the classical von Karman model [11–15], with axial stain truncated to quadratic terms, was developed and applied to geometrical nonlinearity analyses in a straight configuration [16, 17]. This analytical model combines the membrane and bending forces, in which the internal longitudinal force is generated by the end-constraint-induced tensile rigidity. In the proposed treatment, the axial inertia term is deemed negligible and therefore omitted [7, 18]. Such models lead to a resultant nonlinear force described by cubic terms which dominate the hardening effects on all vibration modes [19]. Considering an initial curvature, a modified von Karman model [20] was proposed through two separate equations: one on the transverse motion and another on longitudinal force inside a beam. Analyses show quadratic terms which cause the softening phenomenon of vibration modes [20, 21]. From a different perspective, by integrating all nonlinear terms into one equation, Nayfeh and Mook [16] and Lacarbonara et al. [22] developed an integral–differential condensation model with the consideration of nonlinear stretching. The work clearly illustrates that the initial curvature generates quadratic terms instead of cubic terms in the system equation. The ultimate hardening/softening is determined by the domination level of these competing terms. Meanwhile, Yi et al. [23] investigated the nonlinear dynamic behaviors and modal interactions in the presence of elastic supports, in which hardening/softening can coexist. Qiao et al. [6] utilized a refined multi-scale method to simulate the hardening–softening transition with the consideration of the initial curvature. Analyses show that a near-transition region appears where the competing nonlinearities from hardening/softening balance each other. Meanwhile, Ghayesh et al. [4] exploited coupled stress tensor in a micro-beam structure, with results showing that the softening induced by the initial curvature can turn into hardening with increasing forcing level.

Different with end-constrained structures, i.e., clamped or pinned boundaries, a free boundary in a cantilever beam would cause the shortening effect [9], which creates intriguing problems. More specifically, the strain along the neural axis of the beam becomes zero and the coupling between the transverse and longitudinal motions of the beam is enhanced. Together with the initial curvature, significant nonlinear inertia effect is expected to surge to significantly impact on the nonlinear dynamic behaviors of the system. Note this inertia effect has traditionally been ignored in an end-constrained beam. Meanwhile, as to be illustrated later, the consideration of the inertia effect also creates additional difficulties in solving the system dynamic equations. Past attempts to address similar problems were only based on straight cantilever beams using geometrically exact beam models [1, 9, 24–27]. In particular, an inextensible condensation model on a straight cantilever beam [7, 9, 26, 28–31] shows cubic nonlinear terms arising from the nonlinear stiffness and nonlinear inertia, whose relative dominance levels ultimately determine the modal hardening or softening. In general, nonlinear inertia effect is commonly considered to dominate high frequencies in a uniform beam, which is accountable for the modal softening [16], while nonlinear stiffness has noticeable effects on the first vibration mode through producing hardening effect, as verified both theoretically [9, 28–30] and experimentally [32–34]. More recently, Thomas et al. [29] extended the inextensible model to a rotating

cantilever beam and discussed distinctions between von Karman's theory and the inextensible model. Considering the rotation-induced centrifugal force, a reduced order model was applied to investigate the hardening/softening phenomena. With increasing rotating speed, the rotary effect, coupled with the nonlinear stiffness and nonlinear inertia, results in a hardening–softening transition for the first mode, and an enhanced softening effect for higher order modes. Meanwhile, Farokhi et al. [34] utilized a geometrically exact model to investigate the scenario of extremely large motion in cantilevers with experimental validations, and the reported results emphasized the deficiency of the well-known truncated inextensible model [9, 26] in this extreme case. Amabili et al. [35] considered shear effects and rotary inertia, which may become more important than nonlinear inertia in a thick cantilever beam. Related studies investigated pipes conveying fluid [36, 37], inextensible plates [38] and other structures [39–43]. Exploiting existing literature, it is felt that apart from a few analyses using finite element models [44–46] and non-condensation analytical models [47, 48] on curved cantilevers, there is a lack of inextensible condensation model as well as a clear understanding of the inertia-induced nonlinear features in an initially curved cantilever beam.

The aforementioned challenges are also accompanied by some specific needs and difficulties associated with the numerical implementation of the model, particularly in terms of discretization and numerical solver development. In fact, proper numerical treatments are needed to cope with the large deformation and inertia-induced nonlinearity terms, which are distributed over the entire structure. On account of this, geometrical nonlinearities, from a modal viewpoint, can be regarded as the result of nonlinear coupling of linear modes [7], which carry clear physical meaning in real life and commonly used as discrete basis in modal approach. The popular technique known as reduced-order model (ROM) [7, 29, 49] can then be applied to construct semi-discrete system equations to mimic/simulate nonlinear complexity in a full order model. Nonlinear frequency response (NFR) curves, backbones and nonlinear normal modes (NNMs) can be numerically solved by asymptotic numerical method (ANM) combined with harmonic balance (HB) method [7, 29, 34, 49, 50]. This approach, though widely used in geometrical nonlinearity analysis with great success, suffers from two drawbacks. The first one is related to ROM, which usually requires a prohibitive number of linear modes to reach convergence, most of them having natural frequencies out of the frequency band of interest. The second issue relating to ANM is the need for recasting the nonlinear terms into quadratic order by introducing auxiliary variables and additional equations, in which the second-order PDEs are transformed to the first order, for which a sufficiently large number of harmonics are required in harmonic balance procedure [51]. As to be demonstrated later in this paper, both limitations are detrimental for the problem to be investigated in this paper, since both the free end of the cantilever beam and its initial curvature would jeopardize the applicability of these techniques. Although conventional HB continuation method (based on alternating frequency/time procedure) [19, 52, 53] can be directly applied to semi-discretized equations, no attempt has been made so far to cope with nonlinear inertia terms using this method, which is also one of the problems to be addressed in this work through the proposal of a dedicated numerical technique. The generalized-α method [54] (one of the time-integration methods), which is conventionally used to confirm the frequency domain results, is very time-consuming, and such method is sensitive to geometrical nonlinearities [29]. This problem also needs to be tackled, which is accomplished in the later part of this paper by introducing an operator splitting (OS) method in the Newton iteration procedure.

Motivated by the aforementioned challenges, this paper targets a threefold objective: (a) to propose a geometrically exact inextensible condensation model on a curved cantilever beam; (b) to modify the HB continuation method and the generalized-α method in iteration procedure on account of inertia terms and (c) to explore salient nonlinear dynamic features of the structure with particular emphasis on the effects of the nonlinear inertia enhanced by the curvature and the free boundary of the beam.

The rest of the paper is organized as follows. The proposed theoretical formulation is first presented. A set of modified numerical methods is then proposed to cope with the numerical problems arising from the inertia effects. The established model is compared with a linear finite element (FE) model to validate the linear features of the model on the one hand and to assess the simplification assumptions being made in the development of the nonlinear model so that its

applicable range can be established on the other hand. Discussions on the stiffness and inertia terms induced by the initial curvature are then carried out. Numerical analyses are then conducted to elucidate the hardening/softening phenomena as well as the influence of the initial curvature. Results show that the first mode undergoes transition from hardening to softening with increasing initial curvature, while the higher order modes exhibit significant asymmetry with respect to frequencies.

2 Inextensible condensation model with initial curvature

We consider a highly flexible and initially curved cantilever beam, which undergoes transverse flexural vibration coupled to the longitudinal motion along its length direction. Due to the free end, large deformation is induced which leads to non-negligible geometrical nonlinearity and compelling nonlinear stiffness and inertia effects. The initial curvature of the beam would further enrich the nonlinear behaviors of the structure as well as the complexity in their analyses. After a brief recap on the geometrically exact model, a novel inextensible condensation model for a cantilever with initial curvature is developed in this section.

2.1 Recap on geometrically exact model

For the completeness of the paper, the geometrically exact model is briefly recalled hereafter. As shown in Fig. 1, three coordinate systems are adapted to describe the geometric deformations of a curved beam segment. As the reference frame, Cartesian coordinate ab is used to define the local rotating coordinates xy and $\xi\eta$. Before the beam segment is deformed, the undeformed coordinate xy is fixed to the structure and rotates in the plane alongside the initial curve of the beam segment, whereas the deformed coordinate $\xi\eta$ specifies the segment motion with respect to xy. Their unit vectors are denoted, respectively, by $(\mathbf{i}_a, \mathbf{i}_b)$,$(\mathbf{i}_x, \mathbf{i}_y)$ and $(\mathbf{i}_1, \mathbf{i}_2)$ in the 2D plane. The location of an arbitrary point p on the beam is defined as $\mathbf{D}_p = A\mathbf{i}_a + B\mathbf{i}_b$ in the ab coordinate, and the point q is $\mathbf{D}_q = \mathbf{D}_p + \mathbf{D}'_p ds$ through infinitesimal distance ds, which gives

$$\mathbf{i}_x = \mathbf{D}'_p = A'\mathbf{i}_a + B'\mathbf{i}_b, \quad \mathbf{i}_y = -B'\mathbf{i}_a + A'\mathbf{i}_b \tag{1}$$

where $(\cdot)' = \partial(\cdot)/\partial s$ is the derivative with respect to the arclength s, and the module of $\mathbf{i}_x$ follows $A'^2 + B'^2 = 1$ whose first derivative follows $A'A'' + B'B'' = 0$. The rotation angle between the reference and the undeformed coordinates is φ_3 calculated by $\cos\varphi_3 = \mathbf{i}_x \cdot \mathbf{i}_a = A'$ and $\sin\varphi_3 = \mathbf{i}_x \cdot \mathbf{i}_b = B'$, of which the derivative with respect to s is the initial curvature k_3,

$$k_3 = \varphi'_3 = A'B'' - B'A'' \tag{2}$$

Combining Eqs. (1), (2), and the above-mentioned relations of $\mathbf{i}_x$, the derivatives of $(\mathbf{i}_x, \mathbf{i}_y)$ write

$$\mathbf{i}'_x = k_3\mathbf{i}_y, \quad \mathbf{i}'_y = -k_3\mathbf{i}_x \tag{3}$$

Unlike the conventionally global description of displacements in the reference coordinate system, the co-rotational frame fastens deformed beam segment to the deformed coordinate without relative motion. The local displacement is therefore described by (u, v), which is the distance between $\xi\eta$ coordinate with xy coordinate. The end points $\hat{p}$, $\hat{q}$ of the deformed segment are represented by $\mathbf{D}_{\hat{p}} = \mathbf{D}_p + u\mathbf{i}_x + v\mathbf{i}_y$, $\mathbf{D}_{\hat{q}} = \mathbf{D}_{\hat{p}} + \mathbf{D}'_{\hat{p}} ds$, based on which the unit vector $\mathbf{i}_1$ of the deformed coordinate is expressed by

$$\mathbf{i}_1 = \frac{\mathbf{D}'_{\hat{p}}}{(1+e)ds} = \frac{1+u'-vk_3}{1+e}\mathbf{i}_x + \frac{v'+uk_3}{1+e}\mathbf{i}_y \tag{4}$$

where e is the axial strain along the undeformed neutral axis, and $\mathbf{i}_1$ is orthogonal to $\mathbf{i}_2$, i.e., $\mathbf{i}_1 \cdot \mathbf{i}_2 = 0$. Projecting $\mathbf{i}_1$ to xy axes and calculating its module, one obtains

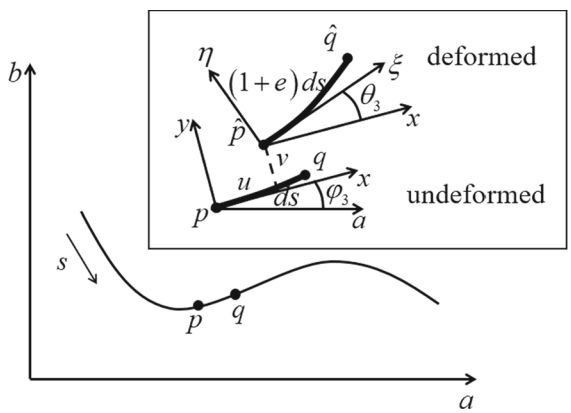

Fig. 1 Definition of coordinate systems and relationship between the undeformed and deformed beam segments

$$\cos\theta_3 = \frac{1+u'-vk_3}{1+e}, \quad \sin\theta_3 = \frac{v'+uk_3}{1+e} \tag{5}$$

$$e = \sqrt{(1+u'-vk_3)^2+(v'+uk_3)^2} - 1 \tag{6}$$

where θ_3 is the deformed angle between $\mathbf{i}_1$ and $\mathbf{i}_x$. Eq. (5) shows that the initial curvature affects the deformation of the beam through orthogonal components like vk_3, and then, causes changes in the bending as well as the stretching properties different from a straight beam.

A flexible and thin structure would experience large deformation but small strain. In this case, it has been demonstrated that [29] engineering strains, consistent linearization of Green–Lagrange strains and Biot-Jaumann strains [1, 55] are identical in an Euler–Bernoulli beam. Consider a cantilever beam with a length L, a cross sectional area A, moment of inertia I, made of homogeneous and isotropic elastic material of density ρ, Young's modulus E. For the bending-dominant oscillations, the normal strains ε_{11},ε_{22} and shear strain ε_{12} on the cross section write

$$\varepsilon_{11} = e - y\theta_3', \quad \varepsilon_{12} = \varepsilon_{22} = 0 \tag{7}$$

which gives the normal stress $\sigma_{11} = E\varepsilon_{11}$. By integrating the normal stress over the cross section A, the longitudinal internal force F_1 and the bending moment M can be obtained as

$$F_1 = \int_A \sigma_{11} dA = EAe, \quad M = -\int_A \sigma_{11} y dA = EI\theta_3' \tag{8}$$

which can lead to the transverse internal force $F_2 = -M'/(1+e)$ through moment balance equation by neglecting the rotating inertia [9]. Since the accelerations $\mathbf{a} = (\ddot{u}, \ddot{v})$ are defined in xy coordinate, internal forces are projected to $(\mathbf{i}_x, \mathbf{i}_y)$ giving

$$\begin{aligned}\mathbf{F} &= F_x\mathbf{i}_x + F_y\mathbf{i}_y \\ &= (F_1\cos\theta_3 - F_2\sin\theta_3)\mathbf{i}_x \\ &\quad + (F_1\sin\theta_3 + F_2\cos\theta_3)\mathbf{i}_y\end{aligned} \tag{9}$$

Applying Newton's second law $d\mathbf{F} = mds \cdot \mathbf{a}$ to an infinitesimal segment ds of an initially curved beam, one has

$$(F_1\cos\theta_3 - F_2\sin\theta_3)' - k_3(F_1\sin\theta_3 + F_2\cos\theta_3) = m\ddot{u} \tag{10}$$

$$(F_1\sin\theta_3 + F_2\cos\theta_3)' + k_3(F_1\cos\theta_3 - F_2\sin\theta_3) + f_{ext} = m\ddot{v} \tag{11}$$

where $m = \rho A$ and f_{ext} is the external force applied to the transverse direction of the beam. Note that the above governing equations obtained by Newton's second law could also be derived from extended Hamilton principle [56] for Euler–Bernoulli beam vibrating in the xy plane. At the end of the curved cantilever beam fixed at $s = L$, boundary conditions write

$$\begin{aligned} &u = v = \theta_3 = 0, \quad &&at\ s = L, \\ &F_x = F_y = M = 0, \quad &&at\ s = 0. \end{aligned} \tag{12}$$

2.2 Shortening effect and assumptions made for inextensible condensation model

Compared with an end-constrained beam, a cantilever beam with a free boundary bears no axial strain along its central line, called neutral line, i.e., $e = 0$. The longitudinal displacement is coupled with the transverse displacement through Eq. (6) and expressed as

$$u' = \sqrt{1-(v'+uk_3)^2} - 1 + vk_3 \tag{13}$$

$$u = -\int_s^L \left(\sqrt{1-(v'+uk_3)^2} - 1 + vk_3\right) ds \tag{14}$$

by using $u_L = 0$ at the constrained end $s = L$. Analytical solution of u is not available even though v is known. We herein assume that in the bending dominant oscillation, the transverse displacement v and its derivative v' have greater impact than uk_3 on calculation of the longitudinal displacement u in Eq. (14). Omitting uk_3 in the presence of v' with moderate initial curvature or local curvature (an assumption whose validity and the applicable range are to be assessed later), one has

$$u \approx -\int_s^L \left(\sqrt{1-v'^2}-1+vk_3\right)ds \approx \int_s^L \left(\frac{1}{2}v'^2-vk_3\right)ds \tag{15}$$

by keeping those terms up to quadratic order through Taylor expansion. Compared to a straight configuration, the longitudinal displacement u reaches the first-order magnitude because of the initial curvature effect, which means that the coupled motion could be enhanced, either by the magnitude of k_3 or the curved length. Considering the force-free condition $F_x = 0$ at $s = 0$ and neglecting $F_1 \sin\theta_3$ in the presence of $F_2 \cos\theta_3$ as a higher order term, the internal longitudinal force, from Eq. (10), can be obtained as

$$F_1 = \frac{1}{\cos\theta_3}\left[\int_0^s (m\ddot{u}+F_2\cos\theta_3 k_3)ds + F_2\sin\theta_3\right] \tag{16}$$

Equation (16) shows the involvement of the nonlinear inertia in the beam vibration. Meanwhile, the initial curvature as well as the curved length affect both the nonlinear inertia and nonlinear stiffness. Substituting Eqs. (15) and into Eq. (11), assuming a constant initial curvature k_3 and expanding all the terms up to the cubic order, one has the full set of condensed dynamic equation which governs the vibration of the cantilever expressed as

$$\begin{aligned} &m\ddot{v}+c\dot{v}+(EIv'')''+k_3^2(EIv)''+k_3\left[k_3EI\left(v''+vk_3^2\right)\Big|_0^s\right]+k_3\int_0^s m\int_s^L \ddot{v}k_3 dsds \\ &+\left\{\begin{array}{l}\frac{1}{2}\left\{\left[EIv'^2\left(v''+vk_3^2-k_3\right)\right]'+v'^2\left[EI\left(v''+vk_3^2\right)\right]'+2v'\left[k_3EI\left(v''+vk_3^2-\frac{1}{2}v'^2k_3\right)\Big|_0^s\right]\right\}' \\ \qquad +k_3\int_0^s EI\left(v''+vk_3^2\right)v'v''k_3ds-\frac{1}{2}k_3\left(k_3^2EIv'^2\Big|_0^s\right)\end{array}\right\} \\ &-\left(v'\int_0^s m\int_s^L\left(\dot{v}'^2+v'\ddot{v}'-\ddot{v}k_3\right)dsds\right)'-k_3\int_0^s m\int_s^L\left(\dot{v}'^2+v'\ddot{v}'\right)dsds \\ &=f_{ext}\end{aligned} \tag{17}$$

Note the above equation contains all linear and nonlinear effects in the system, which describes the full dynamics of the system in the most comprehensive and coupled manner. It is therefore the key equation to be further exploited in this paper. More specifically, the equation explicitly shows that stiffness, inertia, and initial curvature interact with each other both linearly and nonlinearly, giving rise to complex and rich dynamics (to be demonstrated later). More specifically, the first row (comprising the first four terms) presents the linear stiffness $k_3^2(EIv)''+k_3[k_3EI(v''+vk_3^2)|_0^s]$ and inertia $k_3\int_0^s m\int_s^L \ddot{v}k_3 dsds$ induced by the initial curvature. The second and the third rows account for the nonlinear stiffness and nonlinear inertia, respectively, cast into quadratic and cubic order terms. The most significant stiffness terms are connected to the local region of the structure, whereas the double integral of inertia terms takes into account the entire structure. It implies that inertia effect increases with the curved length due its increased portion participating in the vibration. Quadratic order terms appear in the curved cantilever beam, whose nonlinear features rise from the competing effects between the quadratic and cubic order nonlinear terms, which is similar to an end-constrained beam. However, nonlinear stiffness and inertia effects competing inside quadratic order terms are also responsible for the nonlinear dynamic responses.

3 Modified harmonic balance method and generalized-α method

This section proposes an efficient numerical approach, in frequency domain or time domain, respectively, to implement and solve the afore-established model with the consideration of the enhanced inertia effects. With Fourier series truncated to limited terms, HB method, combined with the continuation method, would allow for the calculation of the nonlinear frequency response by balancing the coefficients of the dominant harmonic orders. However, as discussed in Introduction, nonlinear inertia terms are usually handled in ANM by transforming the second-order PDEs to the first order through introducing additional equations, which requires sophisticated mathematic treatment especially for systems with initial curvature. Besides, analytical mode shape functions are seldom available for complex structures, for which we have to resort to FEM. Therefore, we hereafter combine the HB continuation method with FEM. This turns out to be possible since, thanks to the inextensible condensation model, the nonlinear inertia terms are explicitly expressed, which allows proper modifications on the Jacobian matrix, as to be detailed in Sect. 3.1.

In a slightly different perspective, the generalized-α method is often used in nonlinear analyses. However, nonlinear systems usually require sufficiently small time steps, which becomes exorbitantly demanding in the present inertia-dominant system with initial curvature. Thomas et al. [29] opined that time evaluations should be carried out by using very small time steps and stepped-sine excitation to reach convergent results. This proved to be extremely time-consuming (typically 9 million time increment in a single curve) and sensitive to geometrical nonlinearities. To achieve efficient simulation under the proposed modeling umbrella, we propose a splitting technique in the iteration stage of the Newton–Raphson method at each time step, to be detailed in Sect. 3.2.

To discretize Eq. (17), the finite element method is followed by Galerkin procedure to build semi-discrete governing equation, with its element vector expressed as

$$\int_0^{l_e} [N]^T \left[m\ddot{v} + c\dot{v} + (EIv'')''\right] ds_e = \int_0^{l_e} [N]^T f_{ext} ds_e - \int_0^{l_e} [N]^T f_{int}\left(v, v', v'', \ddot{v}, \dot{v}', \ddot{v}'', k_3\right) ds_e \tag{18}$$

where $[N]$ is the cubic shape function of Hermitian element containing four degrees of freedom (DOFs),l_e is the element length, superscript T is the vector transpose operator. The continuous variable v in an element is approximated by $v = [N][d_e]$, in which $[d_e] = [v_0\ v_0'\ v_1\ v_1']^T$ is the element vector of the DOF. The global mass, damping as well as stiffness matrices are then constructed for left side terms of Eq. (18), with the clamped boundary conditions imposed [57]. All other portions including curvature-induced linear and nonlinear terms are gathered into a resultant force f_{int} vector, which allows for the treatment of piecewise constant initial curvature for locally curved configuration.

3.1 Modified harmonic balance method

Based on Eq. (18), the corresponding general non-autonomous nonlinear dynamic system with N DOFs is cast into the following general form

$$\mathbf{M}\ddot{\mathbf{x}} + \mathbf{C}\dot{\mathbf{x}} + \mathbf{K}\mathbf{x} + \mathbf{f}_{int}(\mathbf{x}, \dot{\mathbf{x}}, \ddot{\mathbf{x}}) = \mathbf{f}_{ext}(\omega, t) \tag{19}$$

in which all internal force terms are regrouped in to $\mathbf{f}_{int}(\mathbf{x}, \dot{\mathbf{x}}, \ddot{\mathbf{x}}),\mathbf{x}(t)$ and $\mathbf{f} = \mathbf{f}_{ext}(\omega, t) - \mathbf{f}_{int}(\mathbf{x}, \dot{\mathbf{x}}, \ddot{\mathbf{x}})$ in Eq. (19) are approximated by Fourier series truncated to the N_H-th harmonic as

$$\mathbf{x}(t) = \frac{\mathbf{c}_0^x}{\sqrt{2}} + \sum_{k=1}^{N_H} \left(\mathbf{s}_k^x \sin(k\omega t) + \mathbf{c}_k^x \cos(k\omega t)\right) \tag{20}$$

$$\mathbf{f}(t) = \frac{\mathbf{c}_0^f}{\sqrt{2}} + \sum_{k=1}^{N_H} \left(\mathbf{s}_k^f \sin(k\omega t) + \mathbf{c}_k^f \cos(k\omega t)\right) \tag{21}$$

The coefficients are gathered into the $(2N_H + 1)N \times 1$ vectors as

$$\mathbf{z} = \left[\left(\mathbf{c}_0^x\right)^T \quad \left(\mathbf{s}_1^x\right)^T \quad \left(\mathbf{c}_1^x\right)^T \quad \cdots \quad \left(\mathbf{s}_{N_H}^x\right)^T \quad \left(\mathbf{c}_{N_H}^x\right)^T\right]^T \tag{22}$$

$$\mathbf{b} = \left[\left(\mathbf{c}_0^f\right)^T \quad \left(\mathbf{s}_1^f\right)^T \quad \left(\mathbf{c}_1^f\right)^T \quad \cdots \quad \left(\mathbf{s}_{N_H}^f\right)^T \quad \left(\mathbf{c}_{N_H}^f\right)^T \right]^T \tag{23}$$

Substituting Eqs. (20–23) into Eq. (19) and following the standard Fourier–Galerkin balance procedure, a new target function $\mathbf{h}$ [52] depending on Fourier coefficients gives

$$\mathbf{h}(\mathbf{z}, \omega) = \mathbf{A}(\omega)\mathbf{z} - \mathbf{b}(\mathbf{z}) = \mathbf{0} \tag{24}$$

with

$$\mathbf{A} = \nabla^2 \otimes \mathbf{M} + \nabla \otimes \mathbf{C} + \mathbf{I}_{2N_H+1} \otimes \mathbf{K} \tag{25}$$

where $\mathbf{A}$ is $(2N_H+1)N \times (2N_H+1)N$ matrix for linear system;$\otimes$ stands for the Kronecker tensor product;∇ and ∇^2 are gradient and Laplace operator matrices defined in [52]. The above equation is settled once the force coefficient vector $\mathbf{b}$ is provided. Through displacement–force relationship in time domain, alternating frequency/time method [58] and trigonometric collocation method are applied through Fast Fourier Transform (FFT) procedure, which gives

$$\mathbf{z} \xrightarrow{FFT^{-1}} \tilde{\mathbf{x}} = \mathbf{\Gamma}(\omega)\mathbf{z} \rightarrow \tilde{\mathbf{f}} \xrightarrow{FFT} \mathbf{b}(\mathbf{z}) = \mathbf{\Gamma}^+(\omega)\tilde{\mathbf{f}} \tag{26}$$

where $\tilde{\mathbf{x}} = [x_1(\tilde{\mathbf{t}}) \ \cdots \ x_N(\tilde{\mathbf{t}})]$ and $\tilde{\mathbf{f}} = [f_1(\tilde{\mathbf{t}}) \ \cdots f_N(\tilde{\mathbf{t}})]$ contain N_T time samples $\tilde{\mathbf{t}} = [t_1 \ \cdots \ t_{N_T}]$ in each DOF, and the superscript $+$ stands for the Moore–Penrose pseudoinverse. The linear operator matrix for inverse Fourier transform of displacement writes

$$\mathbf{\Gamma}(\omega) = \Big[\mathbf{I}_N \otimes [0 \cdot \tilde{\mathbf{t}}]^T \mathbf{I}_N \otimes [\sin(\omega\tilde{\mathbf{t}})]^T \quad \mathbf{I}_N \otimes [\cos(\omega\tilde{\mathbf{t}})]^T \quad \cdots \quad \mathbf{I}_N \otimes [\sin(N_H\omega\tilde{\mathbf{t}})]^T \quad \mathbf{I}_N \otimes [\cos(N_H\omega\tilde{\mathbf{t}})]^T \Big] \tag{27}$$

and similar matrices for velocity and acceleration are

$$\dot{\mathbf{\Gamma}}(\omega) = \Big[\mathbf{I}_N \otimes [0 \cdot \tilde{\mathbf{t}}]^T \quad \mathbf{I}_N \otimes \omega[\cos(\omega\tilde{\mathbf{t}})]^T \quad \mathbf{I}_N \otimes \omega[-\sin(\omega\tilde{\mathbf{t}})]^T \cdots \mathbf{I}_N \otimes N_H\omega[\cos(N_H\omega\tilde{\mathbf{t}})]^T \quad \mathbf{I}_N \otimes N_H\omega[-\sin(N_H\omega\tilde{\mathbf{t}})]^T \Big] \tag{28}$$

$$\ddot{\mathbf{\Gamma}}(\omega) = -\Big[\mathbf{I}_N \otimes [0 \cdot \tilde{\mathbf{t}}]^T \quad \mathbf{I}_N \otimes \omega^2[\sin(\omega\tilde{\mathbf{t}})]^T \quad \mathbf{I}_N \otimes \omega^2[\cos(\omega\tilde{\mathbf{t}})]^T \quad \cdots \quad \mathbf{I}_N \otimes (N_H\omega)^2[\sin(N_H\omega\tilde{\mathbf{t}})]^T \quad \mathbf{I}_N \otimes (N_H\omega)^2[\cos(N_H\omega\tilde{\mathbf{t}})]^T \Big] \tag{29}$$

The Newton–Raphson method is utilized to reach the final solution iteratively through the calculation of the Jacobian matrix, which has impact on stability and accuracy of solution specific to inertia-induced feature. Using the chain rule, the Jacobian matrix of Eq. (24) with respect to $\mathbf{z}$ is written as

$$\begin{aligned} \frac{\partial \mathbf{h}}{\partial \mathbf{z}} = \mathbf{A} - \frac{\partial \mathbf{b}}{\partial \mathbf{z}} = \mathbf{A} - \frac{\partial \mathbf{b}}{\partial \tilde{\mathbf{f}}}\frac{\partial \tilde{\mathbf{f}}}{\partial \mathbf{z}} = \mathbf{A} - \frac{\partial \mathbf{b}}{\partial \tilde{\mathbf{f}}}\left(\frac{\partial \tilde{\mathbf{f}}}{\partial \tilde{\mathbf{x}}}\frac{\partial \tilde{\mathbf{x}}}{\partial \mathbf{z}} + \frac{\partial \tilde{\mathbf{f}}}{\partial \dot{\tilde{\mathbf{x}}}}\frac{\partial \dot{\tilde{\mathbf{x}}}}{\partial \mathbf{z}} + \frac{\partial \tilde{\mathbf{f}}}{\partial \ddot{\tilde{\mathbf{x}}}}\frac{\partial \ddot{\tilde{\mathbf{x}}}}{\partial \mathbf{z}}\right) \\ = \mathbf{A} - \mathbf{\Gamma}^+\frac{\partial \tilde{\mathbf{f}}}{\partial \tilde{\mathbf{x}}}\mathbf{\Gamma} - \mathbf{\Gamma}^+\frac{\partial \tilde{\mathbf{f}}}{\partial \dot{\tilde{\mathbf{x}}}}\dot{\mathbf{\Gamma}} - \mathbf{\Gamma}^+\frac{\partial \tilde{\mathbf{f}}}{\partial \ddot{\tilde{\mathbf{x}}}}\ddot{\mathbf{\Gamma}} \end{aligned} \tag{30}$$

which includes independent variables related to resultant forces $\mathbf{f}(\mathbf{x}, \dot{\mathbf{x}}, \ddot{\mathbf{x}})$, and inertia effects associated with entire DOFs. Since the stiffness terms are only connected to adjacent DOFs, the matrix $\partial\tilde{\mathbf{f}}/\partial\tilde{\mathbf{x}}$ is sparse and diagonally dominant, which usually has analytical formulation [19]. On the contrary,$\partial\tilde{\mathbf{f}}/\partial\dot{\tilde{\mathbf{x}}}$ and $\partial\tilde{\mathbf{f}}/\partial\ddot{\tilde{\mathbf{x}}}$ are dense matrices because of the integral term in Eq. (17) and numerically approached by finite difference method. However, this approximation approach would slow down the convergence of iteration. To work out partial equations both efficiently and precisely, the eighth-order central difference scheme is adopted to calculate $\partial\tilde{\mathbf{f}}/\partial\tilde{\mathbf{x}}$,$\partial\tilde{\mathbf{f}}/\partial\dot{\tilde{\mathbf{x}}}$ and $\partial\tilde{\mathbf{f}}/\partial\ddot{\tilde{\mathbf{x}}}$. The predicted solution is then corrected by Moore–Penrose continuation method. This is formulated as

$$\begin{aligned} \mathbf{y}_{(i,j+1)} &= \mathbf{y}_{(i,j)} - \mathbf{G}_{y,(i,j)}^{-1}\mathbf{G}_{(i,j)} \\ \mathbf{v}_{(i,j+1)} &= \mathbf{v}_{(i,j)} - \mathbf{G}_{y,(i,j)}^{-1}\mathbf{R}_{(i,j)} \end{aligned} \tag{31}$$

with

$$\mathbf{G} = \begin{bmatrix} \mathbf{h} \\ 0 \end{bmatrix}, \quad \mathbf{J} = [\mathbf{h}_z \quad \mathbf{h}_\omega], \quad \mathbf{G}_y = \begin{bmatrix} \mathbf{J} \\ \mathbf{v}^T \end{bmatrix}, \quad \mathbf{R} = \begin{bmatrix} \mathbf{J}\mathbf{v} \\ 0 \end{bmatrix} \tag{32}$$

by introducing optimization tangent vectors initialized as $\mathbf{v}_{(i,1)} = \mathbf{t}_i$, and $\mathbf{y}_{(i,j)} = [\mathbf{z}_{(i,j)} \quad \omega_{(i,j)}]^T$.

3.2 Operator splitting (OS) technique for the generalized-α method

Time-integration methods are often used in dynamic simulation of cantilevers [29, 30, 59] and additionally become a basic part of more sophisticated algorithms like nonlinear normal modes (NNMs) [60]. In the present case with the presence of initial curvature, the generalized-α method is utilized to calculate the time

history to confirm the frequency domain results. Detailed derivation of this method can be found in Appendix 1.

At each time step, the residual function is calculated as shown in Eq. (55), and approaches to zero in an iterative manner until converged results are reached. However, it is found that the numerical calculation is not stable due to the singularity of Jacobian matrix, which is triggered and amplified by the substantial inertia effects in the beam configuration under investigation here. To tackle the problem of avoiding singular iteration matrix, an OS technique is proposed here. The rationale behind is taking apart a complex function into several simple ones which are stable and easy to solve. The sequential splitting idea is herein proposed and presented as follows.

For $k+1$ th iteration at the time step $i+1$, the residual vector is expressed as

$$\mathbf{r}_{i+1}^{k+1} \approx \mathbf{r}_{i+1}^{k} + \left[\mathbf{S}_L + (1-\alpha_f)\frac{\partial \mathbf{f}_{nl}^{k}}{\partial \mathbf{x}} + \frac{\gamma(1-\alpha_f)}{\beta\Delta t}\frac{\partial \mathbf{f}_{nl}^{k}}{\partial \dot{\mathbf{x}}} + \frac{1-\alpha_m}{\beta\Delta t^2}\frac{\partial \mathbf{f}_{nl}^{k}}{\partial \ddot{\mathbf{x}}}\right]\Delta \mathbf{x}_{i+1}^{k} = \mathbf{0} \tag{33}$$

Taking apart the nonlinear Jacobian matrix and dividing the iteration into 3 steps, by considering the first step $k+1/3$, the residual vector writes

$$\mathbf{r}_{i+1}^{k+\frac{1}{3}} \approx \mathbf{r}_{i+1}^{k} + \left[\mathbf{S}_L + (1-\alpha_f)\frac{\partial \mathbf{f}_{nl}^{k}}{\partial \mathbf{x}}\right]\Delta \mathbf{x}_{i+1}^{k} = \mathbf{0} \tag{34}$$

to obtain the updated value $\mathbf{x}_{i+1}^{k+1/3}$ before calculating the second step $k+2/3$,

$$\mathbf{r}_{i+1}^{k+\frac{2}{3}} \approx \mathbf{r}_{i+1}^{k+\frac{1}{3}} + \left[\mathbf{S}_L + \frac{\gamma(1-\alpha_f)}{\beta\Delta t}\frac{\partial \mathbf{f}_{nl}^{k+\frac{1}{3}}}{\partial \dot{\mathbf{x}}}\right]\Delta \mathbf{x}_{i+1}^{k+\frac{1}{3}} = \mathbf{0} \tag{35}$$

By following the same procedure, the final stage $k+1$ is

$$\mathbf{r}_{i+1}^{k+1} \approx \mathbf{r}_{i+1}^{k+\frac{2}{3}} + \left[\mathbf{S}_L + \frac{1-\alpha_m}{\beta\Delta t^2}\frac{\partial \mathbf{f}_{nl}^{k+\frac{2}{3}}}{\partial \ddot{\mathbf{x}}}\right]\Delta \mathbf{x}_{i+1}^{k+\frac{2}{3}} = \mathbf{0} \tag{36}$$

If $||\mathbf{r}_{i+1}^{k+1}|| \le \varepsilon(\varepsilon = 10^{-6})$, converged results are reached, and one can proceed to the next time step. Overall, this method divides the original expression into three different nonlinear sub-problems, each involving their respective nonlinear Jacobian matrices, and the sub-problem is accordingly solved in sequence. As such, while the Jacobian matrix involving nonlinear stiffness terms being generally diagonally dominant, the ill-condition problem of Jacobian matrix due to nonlinear inertia terms with increasing geometrical nonlinearities is avoided and emerged in the numerical solver. As a result, the splitting procedure improves the accuracy, efficiency and the robustness of the generalized-α method, as demonstrated in Appendix 2.

4 Numerical results and analyses

4.1 Curvature-induced inertia/stiffness effects in linear models

This section focuses on the verification of the proposed model through examining the frequency responses and mode shapes of cantilevers in linear cases, to be used as a benchmark for the subsequent nonlinear analyses. Consistent with the reference solutions [29] provided for in a straight beam configuration, the same geometrical and material parameters are used: length $L = 1$ m, rectangular cross section with a thickness $h = 0.005$ m and width $b = 0.1$ m, Young's modulus $E = 104$ GPa and density $\rho = 4400\,\mathrm{kg/m^3}$. When the beam is initially bended to form an initial curvature, two additional parameters are used for geometry description of the curved part: level of the initial curvature k_3 as defined in Eq. (2) and the curved arc length l_c starting from the free end tip of the beam.

From slightly to largely curved configurations, four cases are first examined as shown in Fig. 2: $(i)k_3 = 0.5\pi, l_c/L = 0.1$; $(ii)k_3 = 0.5\pi, l_c/L = 0.5$; $(iii)k_3 = 0.5\pi, l_c/L = 1$; $(iv)k_3 = \pi, l_c/L = 1$. These

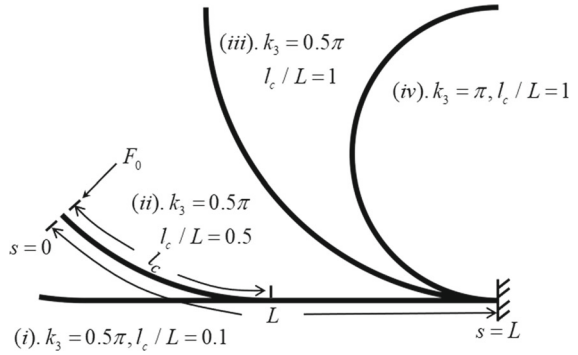

Fig. 2 Definition of the curved configurations for cantilever beam

configurations are also used to clarify the application range of the approximation used during the development of the condensation model in Eq. (15). A free boundary is imposed at $s = 0$, and the other extreme end of the beam is clamped at $s = L$. A concentrated harmonic excitation force with an amplitude F_0 is transversely applied at the free end tip of the beam. Totally 20 uniform elements along the beam are utilized in the proposed model for analyses, and 24 Euler–Bernoulli beam elements are used in the beam interface of COMSOL software to provide linear reference solutions with the consideration of the initial curvature effect. For linear cases, a damping matrix $\mathbf{C} = \eta\mathbf{K}/2\pi f_i$, proportional to the stiffness matrix with a structural damping coefficient η of 0.005, is introduced. Denoting the natural frequency of each mode by f_i, both methods give very consistent values for the first four natural frequencies of the straight cantilever beam, i.e., $f_1 = 3.927$ Hz, $f_2 = 24.644$ Hz,$f_3 = 68.907$ Hz and $f_4 = 135.03$ Hz.

4.1.1 *Linear frequency response*

Linear frequency responses are first calculated using different numerical strategies. The proposed model utilizes the HB method with $N_H = 1$ and Newton iteration $\mathbf{z}^* = \mathbf{z} - \mathbf{h}_z^{-1}\mathbf{h}$, where $\mathbf{z}^*$ is the accurate Fourier coefficient vector when results are converged. Calculated frequencies are equally spaced with $\Delta f = 2$ Hz to cover the range up to 500 Hz. The calculated

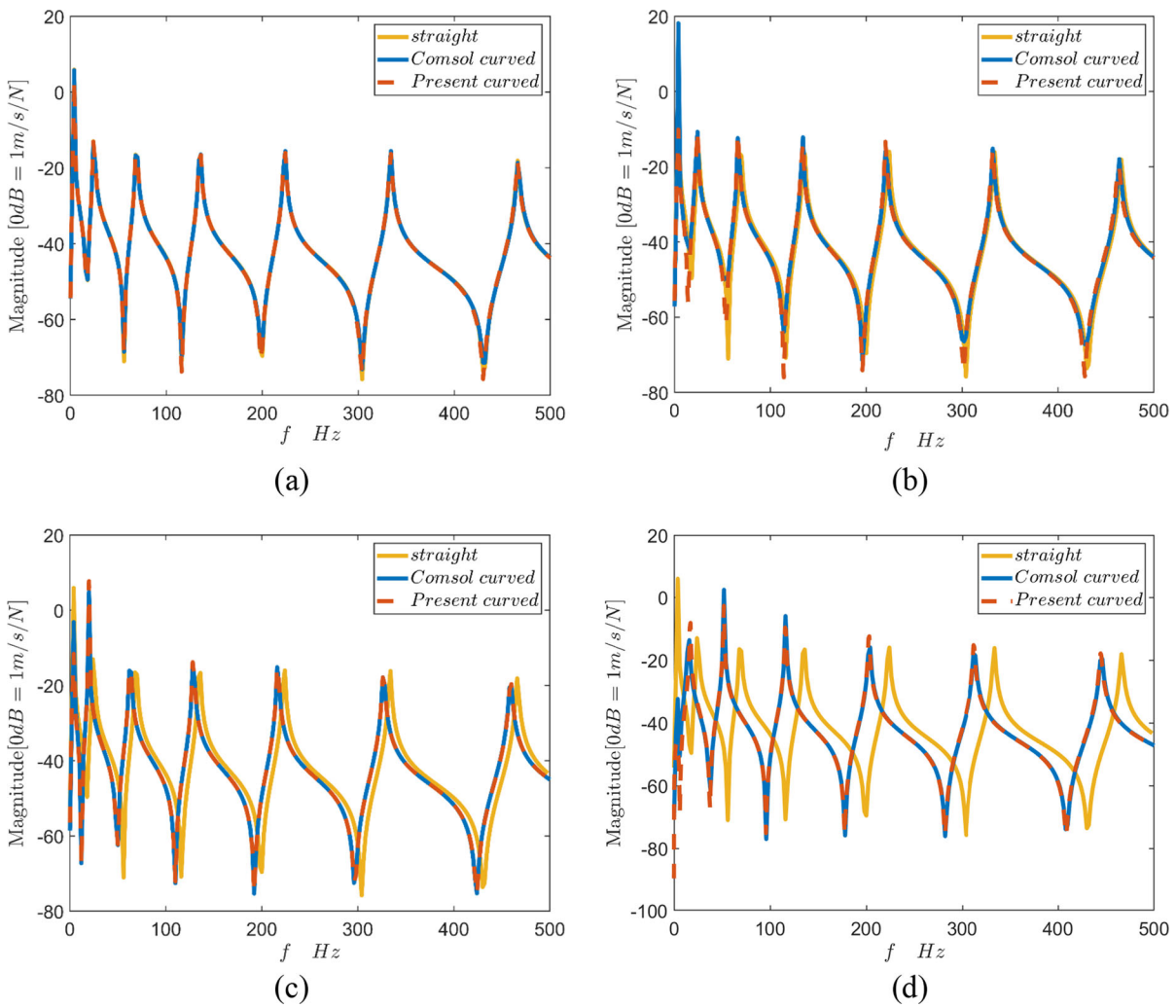

Fig. 3 Linear FRFs at the free end tip. From **a** to **d**: configuration (*i*)–(*iv*), respectively

point mobility of the beams is quantified in terms of $20\log_{10}(\dot{v}/F_0)$ dB, where $\dot{v}$ is the transverse velocity defined in local xy coordinate. Figure 3 depicts the calculated mobilities of both the straight and curved beams with increasing initial deformation. For all four configurations, results show nice agreement between the results obtained from the proposed model and COMSOL (Fig. 3a–d). Upon a very close examination, some barely noticeable differences, especially when the initial deformation becomes severe (e.g., Fig. 3d for a demi-circle), exist but are all within an acceptable error range. This thus validates the linear part of the proposed model.

Cross figure comparisons between Fig. 3a–d, alongside the comparison with the straight beam, allow for the examination of the effects of the initial curvature and the curved arclength on the dynamics of the beams. It can be observed that the differences between the curved beams and the straight beam increase when the beam is more severely curved. By increasing the curved portion of the beam (through increasing either k_3 or l_c), natural frequencies gradually decrease for all modes. Taking the fourth natural frequency as an example, it drops by 2.03 Hz, 6.53 Hz and 19.03 Hz from Fig. 3b–d. Meanwhile, resonance peaks also change with the frequency shift. It can be seen that, compared with the straight beam, the first resonance peak of the curved beam increases in Fig. 3b but decreases again in Fig. 3c and d, and the second to the fourth resonance peaks increase with increased curvature/arclength. All these can be attributed to the curvature, albeit still linear in the present stage, as a result of the coupled motion between the longitudinal and transverse displacements.

4.1.2 *Linear mode shapes*

To further substantiate the above and explain the underlying effects of the initial curvature, Fig. 4 shows the normalized mode shapes of the first three modes in the four curved configurations (*i*)–(*iv*) (as illustrated in Fig. 2). First of all, comparisons of mode shapes show good agreement between the proposed model and COMSOL simulation in terms of modal deformation. Mode shapes, in terms of longitudinal displacement u, are shown in the left column of Fig. 4. It can be observed that the initial curvature effect causes a larger portion of the beam to deform longitudinally, especially within the curved portion. The longitudinally deformed area expands for higher order modes as shown from Fig. 4a–c. It can then be surmised that this phenomenon, coupled with transverse deformation of the beams, would in principle create enhanced inertia effects. Moreover, initial curvature also affects the transverse deformation, as illustrated by the right column in Fig. 4, although variation patterns would be mode-specific. For example, the first mode (Fig. 4a) shows that the largest displacement of configuration (*iv*) no longer occurs at the free end tip of the beam but moves closer to the middle when the initial deformation is large. The second and the third modes, however, show reduced deformation as compared to the tip when initial curvature increases.

4.1.3 *Examination of assumptions and effects of curvature-induced linear stiffness/inertia*

In addition to the verification of the frequency responses and changes in the mode shapes, observations on the longitudinal deformation also testify the efficacy of the piece-wise treatment with constant initial curvature used in proposed model, thus expanding the application range to locally curved configuration. As mentioned above, an approximation is used in Eq. (15) to facilitate the treatment of the longitudinal components so that the condensed model can finally be established. Therefore, it is important to revisit and assess this critical assumption which was used for approximation and at the same time check its validation range. To this end, we re-examine Eq. (13) by applying Taylor expansion and neglecting terms starting from $(uk_3)^2$. This process leads to the truncated expression of u' written as

$$u' = -\frac{1}{2}\left[2v'k_3 \cdot u + v'^2\right] + vk_3 \tag{37}$$

which is then cast into the standard first-order non-homogeneous linear differential equation as

$$u' + v'k_3 \cdot u = -\frac{1}{2}v'^2 + vk_3 \tag{38}$$

The method of variation of constants [61] is then applied to solve Eq. (38) in which the following adjacent homogeneous equation needs to be solved first

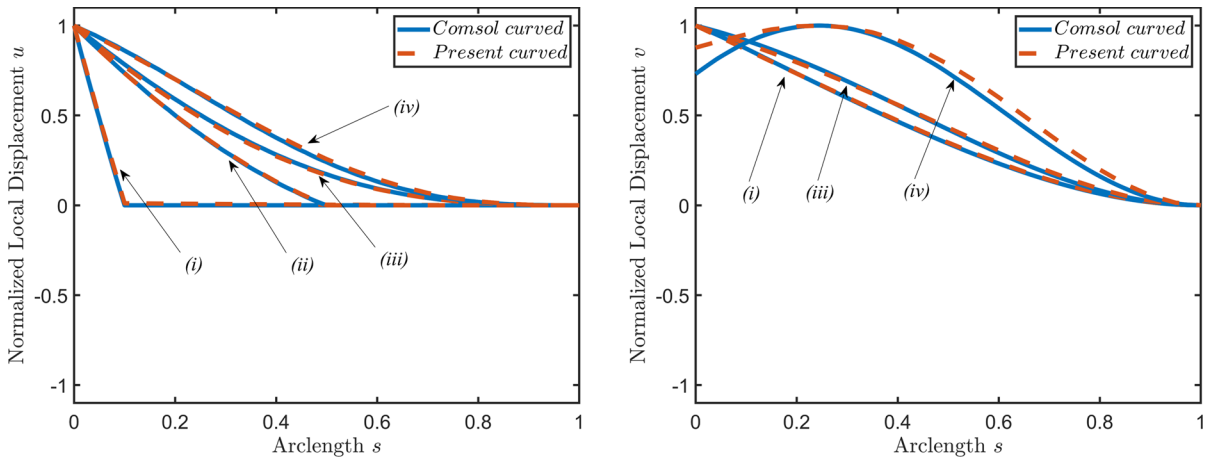

(a) Mode 1

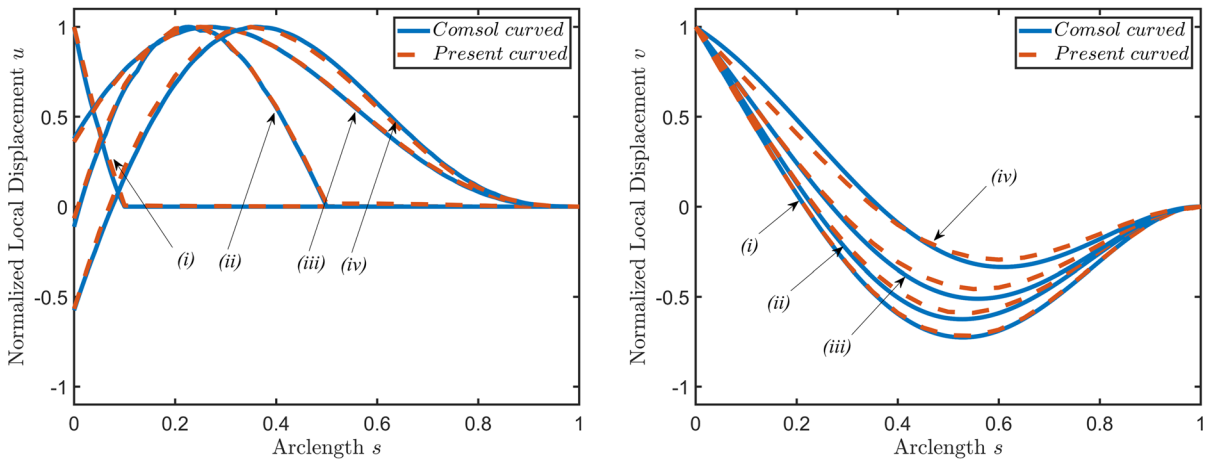

(b) Mode 2

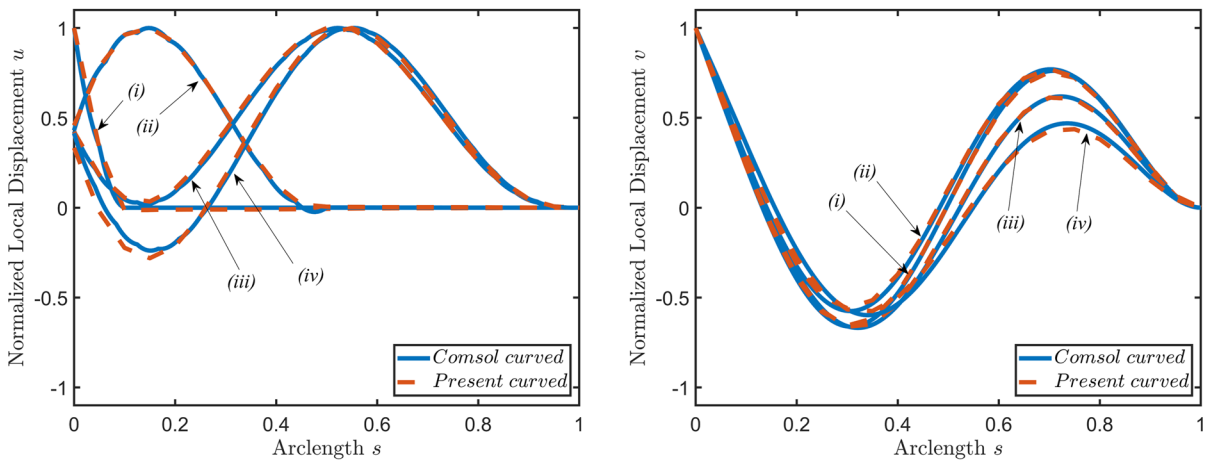

(c) Mode 3

Fig. 4 Normalized mode shapes for curved cantilever beams. Left to right: u, v

$$u' + v'k_3 \cdot u = 0 \tag{39}$$

Integrating the above equation from s to L, the homogeneous solution $\tilde{u}$ writes

$$\tilde{u} = Cu(L)e^{\int_s^L v'k_3 ds} \tag{40}$$

where C is a constant. Then, replacing the constant C with $C(s)$ and substituting $\tilde{u}$ into Eq., the unknown function $C(s)$ can be determined. Substituting $C(s)$ back into $\tilde{u}$, the final general solution, denoted by u_{full}, of the non-homogeneous equation writes

$$u_{full} = e^{\int_s^L v'k_3 ds} \int_s^L \left(\frac{1}{2}v'^2 - vk_3\right) e^{-\int_s^L v'k_3 ds} ds \tag{41}$$

Note the above procedure allows for a more accurate estimation of the longitudinal displacement than the solution u obtained previously based on the approximation made in Eq. (15). To quantify the difference, a relative error factor over the entire beam span is defined as

$$P_1 = \left\| \frac{\int_0^L \|u\| ds - \int_0^L \|u_{full}\| ds}{\int_0^L \|u\| ds} \right\| \times 100\% \tag{42}$$

To introduce noticeable nonlinear effects, the transverse displacement at the free end tip of the beam is set to $v_0 = 50r_g$ for all modes, where r_g is the radius of gyration and defined by $r_g = h/\sqrt{12}$ with a rectangle cross section. In the present case, $v_0 = 0.072$ m. For even larger deformation used in the subsequent analyses, this issue will be commented again in due course. Using the linear mode shapes calculated above as an approximation, the calculated relative error P_1 for the first three modes in all four previous curved configurations is illustrated in Fig. 5. It follows that, the slightly curved configuration (i) generates a very small error for all three modes, typically below 1%. As the beam is bent more severely, error increases. Nevertheless, even for the largest curved configuration (iv), the relative error is still capped below 8%, which is still acceptable. Therefore, the assumption used is deemed valid for all four configurations, even for the last one which is a severely curved semi-circle beam.

As presented in the governing equation (Eq. 17), the initial curvature affects the linear terms through a combined stiffness term and an inertia term, denoted by

$$\begin{aligned} k_{IC} &= k_3^2(EIv)'' + k_3\left[k_3 EI\left(v'' + vk_3^2\right)\Big|_0^s\right], \\ m_{IC} &= k_3 \int_0^s m \int_s^L \ddot{v}k_3 ds ds \end{aligned} \tag{43}$$

Their respective impacts on the linear system response are demonstrated. To this end, k_{IC} and m_{IC} are separately considered for the extreme case of the curved configuration (iv). The calculated FRFs are depicted in Fig. 6, which shows that both curvature-induced stiffness and inertia terms cause a reduction in the resonant frequencies, resulting in the ultimate differences between the straight and curved beams. A closer examination suggests that the peak shift caused by the curvature-induced stiffness and inertia is roughly the same starting from the third to higher order modes, although differences are noticeable on

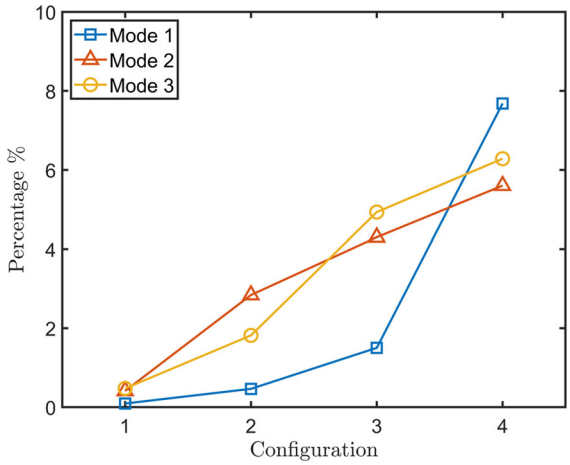

Fig. 5 P_1 for different curved configurations

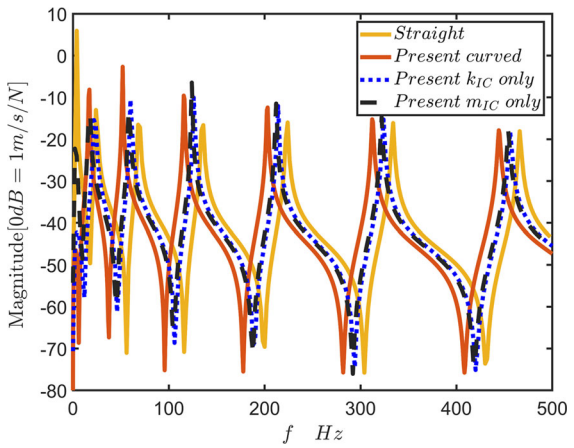

Fig. 6 The initial curvature effect of linear stiffness and inertia

the first two modes. More specifically, for the second mode, the inertia-induced effect affects more the second resonant frequency, while the stiffness-induced effect has a greater impact on the resonance peak level of the first mode.

4.2 Nonlinear dynamic features and curvature-induced inertia effect

This section focuses on the numerical simulations and analyses of nonlinear dynamic behaviors of initially curved cantilever beams. The HB continuation method established in Sect. 3.1 is utilized to provide frequency domain results, to be confirmed by the time history of the response signals. Truncated harmonics and time samples for all numerical simulations are set to $N_H = 5$ and $N_T = 64$, respectively. The generalized-α method should adopt a sufficiently high sampling frequency to slowly sweep in time domain, and the corresponding parameters are determined by the concerned frequency range. A damping matrix $\mathbf{C} = 2\eta\omega_0\mathbf{M}$, proportional to the mass matrix, is introduced, i.e.,$\eta = 0.005$ herein. The amplitude of displacement in nonlinear frequency response (NFR) curves writes

$$\text{Displacement} = \frac{c_0^x}{\sqrt{2}} + 0.5\left(\max x(\tilde{\mathbf{t}}) - \min x(\tilde{\mathbf{t}})\right) \tag{44}$$

which considers the rigid body motion $c_0^x/\sqrt{2}$, so that observations of asymmetry behaviors in frequency domain could coincide with the time history.

Numerical simulations on the curved beam in frequency domain are conducted and verified through comparisons with the time history of the system responses. With the initial curvature increasing from $k_3 = 0$(straight beam) to $k_3 = 0.5\pi$ and a curved arclength of $l_c/L = 0.1$, corresponding NFR curves for the first mode are calculated and illustrated in Fig. 7. In this case, the generalized-α method adopts a sampling frequency $f_s = 400$ Hz to sweep from 3.7 Hz to 4 Hz with a rate of 0.01 Hz/ min. The horizontal axis denotes a dimensionless frequency, which is normalized by the first natural frequency of the corresponding straight beam $f_0 = 3.927$ Hz. Note that the straight beam simulations are firstly carried out using the proposed model, whose results have been compared to reference solutions [29]. At 1.5 N excitation level for the straight configuration, Fig. 7a shows that NFR curves obtained by the proposed model agree well with the reference solution. Meanwhile, the observed NFR variation is also in good agreement with the time history responses obtained from frequency sweeping. More importantly, the hardening effect is obvious for the first mode, as a result of dominant level of the nonlinear stiffness effects. As the initial curvature increases in Fig. 7b–d, the resonance frequency gradually decreases while the hardening evolves to softening. Meanwhile, it can be observed that the resonance frequency peaks of the curved beams are all slightly lower than that of the straight beam (with the normalized frequency smaller than 1). From $k_3 = 0$ to $k_3 = 0.4\pi$, the time domain responses corresponding to the sweeping up process are completely enveloped by the NFR curves, and the process is reversible. The situation is, however, different when the initial curvature increases to $k_3 = 0.5\pi$. In fact, Fig. 7d shows that there exist two turning points on the NFR curve for the curved beam. The sweeping up curve jumps around the first turning point to the upper stable branch, while the sweeping down curve would jump around the second turning point so that hysteresis occurs.

Additional numerical studies are conducted for different curved configurations and different forcing levels. Multiple harmonics, as a salient feature in nonlinear dynamic analysis, would better inform on the complex nonlinear behaviors of the system through revealing the energy level of dominant harmonic orders. Therefore, the normalized harmonic coefficient for each order is calculated by

$$\sigma_i = \frac{\phi_i}{\sum_{k=1}^{N_H}\phi_i}, \quad (i = 0, 1, 2, \cdots, N_H) \tag{45}$$

with

$$\phi_0 = \frac{\left|c_0^x\right|}{\sqrt{2}}, \quad \phi_i = \sqrt{(s_i^x)^2 + (c_i^x)^2}, \quad (i = 1, 2, \cdots, N_H)$$

which depends on the excitation frequency and is comprised between 0 and 1.

The same curved configurations as simulated in the above case are examined with the forcing level changing from 0.5 N to 2 N with a step size of $\Delta F = 0.5$ N. Figure 8a displays the NFR curves for the first mode. Comparing the straight configuration

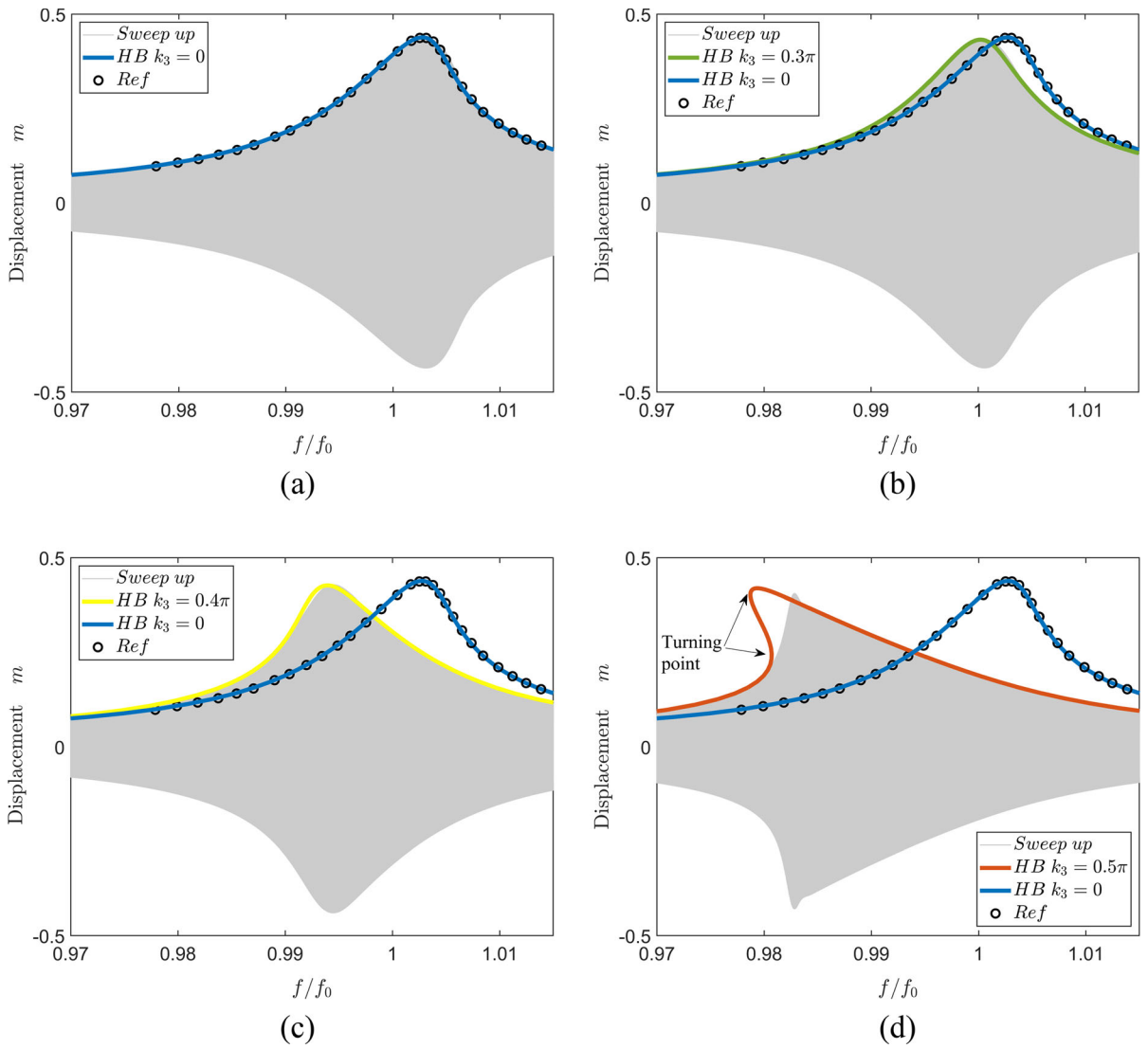

Fig. 7 Comparisons of the HB method and the generalized-α method under 1.5 N force in the first mode for the curved beams with different initial curvature. **a** $k_3 = 0$, **b** $k_3 = 0.3\pi$, **c** $k_3 = 0.4\pi$, **d** $k_3 = 0.5\pi$. Circle: reference solution for the straight beam

results from the HB method with ROM [29] shows nice agreement, even for the largest free-end displacement considered, which amounts to 0.6 m (almost 2/3 of the beam length), with the first five harmonics considered in the current numerical method. For this large displacement, the error indicator P_1 (as defined in Eq. (42)) for this curved configuration is only 0.869%, which is rather small to further confirm the validity of the assumption used in Eq. (15). It can be observed that resonance frequencies decrease with the increasing initial curvature (Fig. 8a). Meanwhile, a similar hardening–softening transition can be observed when the curvature reaches a certain level, as a result of the effective curvature-induced inertia effect. Obviously, a larger excitation level leads to a more significant frequency shift. There exists a specific initial curvature value (between $k_3 = 0.3\pi$ and $k_3 = 0.4\pi$), at which the nonlinear system shows no frequency shift like its linear counterpart. Similar phenomenon, called near-transition, has also been observed in the literature although cases are different [6]. At this specific curvature, various competing nonlinear factors in the system balance each other.

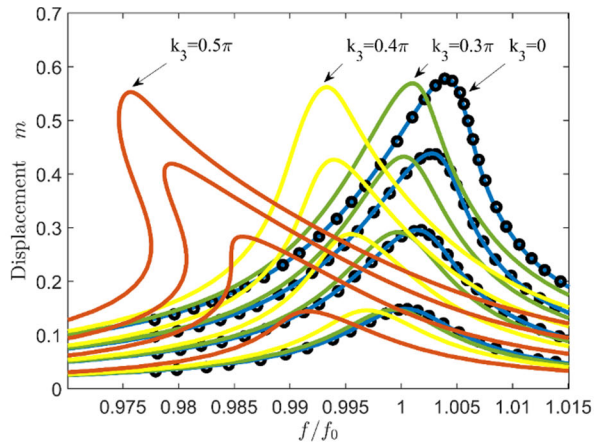
k3=0.5π
k3=0.4π
k3=0.3π
k3=0
Displacement m
f/f0

(a)

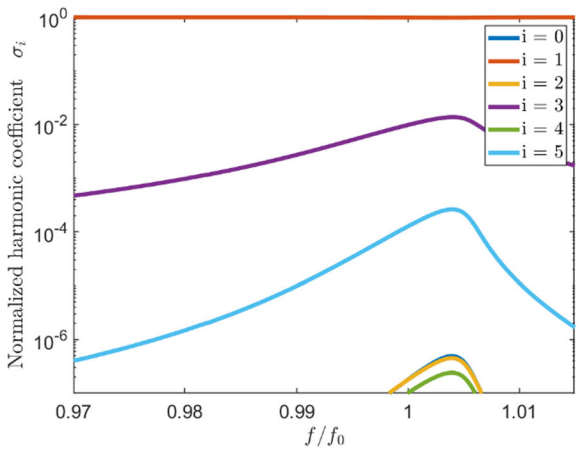
Normalized harmonic coefficient σi
i = 0
i = 1
i = 2
i = 3
i = 4
i = 5
f/f0

(b)

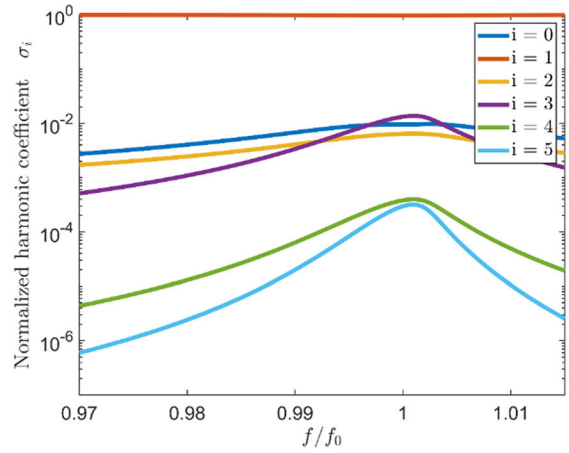
Normalized harmonic coefficient σi
i = 0
i = 1
i = 2
i = 3
i = 4
i = 5
f/f0

(c)

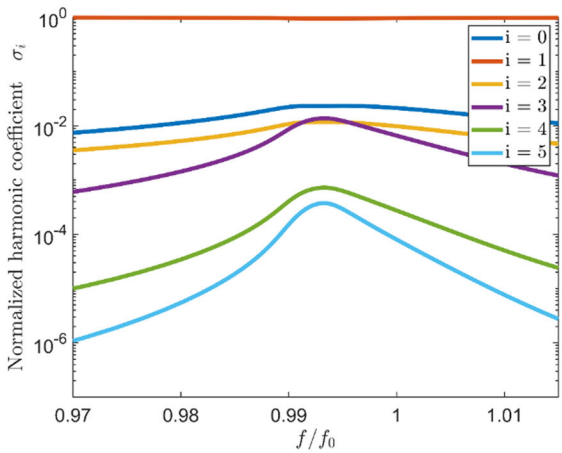
Normalized harmonic coefficient σi
i = 0
i = 1
i = 2
i = 3
i = 4
i = 5
f/f0

(d)

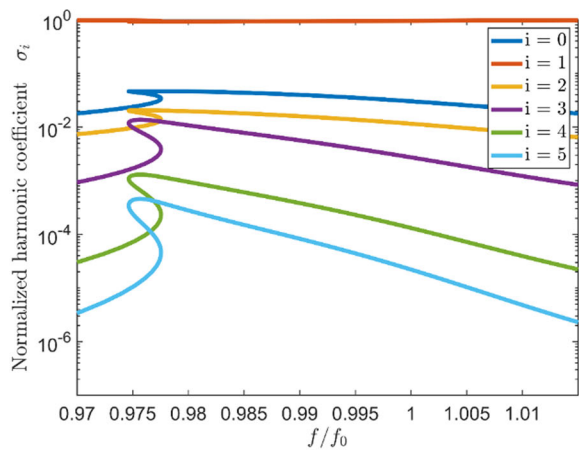
Normalized harmonic coefficient σi
i = 0
i = 1
i = 2
i = 3
i = 4
i = 5
f/f0

(e)

◀**Fig. 8** NFR curves of the first mode with the various initial curvature and excitation level, as well as normalized harmonic coefficients. **a** NFR curves when $F_0 = [0.5N \quad 1N \quad 1.5N \quad 2N]$. Circle: reference solution. The first six harmonic coefficients at the forcing level of 2 *N*: **b** $k_3 = 0$, **c** $k_3 = 0.3\pi$, **d** $k_3 = 0.4\pi$, **e** $k_3 = 0.5\pi$

The normalized harmonic coefficients are logarithmically shown in Fig. 8b–e. Consistent with the NFR curves in Fig. 8a, the appearance of multiple harmonics also confirms the occurrence of the hardening–softening transition. For the straight configuration, Fig. 8b illustrates that the third harmonic coefficient is the largest followed by the fifth one. Note even-order harmonics, which should not exist theoretically, appear because of the computer calculation error, but they have a smaller magnitude than odd-order harmonics. When a small initial curvature is added, it changes system response and induces zero- and even-order harmonics as shown in Fig. 8c. The same pattern basically remains when further increasing the initial curvature, except a slight downshifting of the peak region to lower frequencies as shown in Fig. 8d. It can be observed that the dominant even-order harmonics account for the hardening–softening transition. As to the most severely curved beam (Fig. 8e), a turning point phenomenon similar to that observed in Fig. 8d

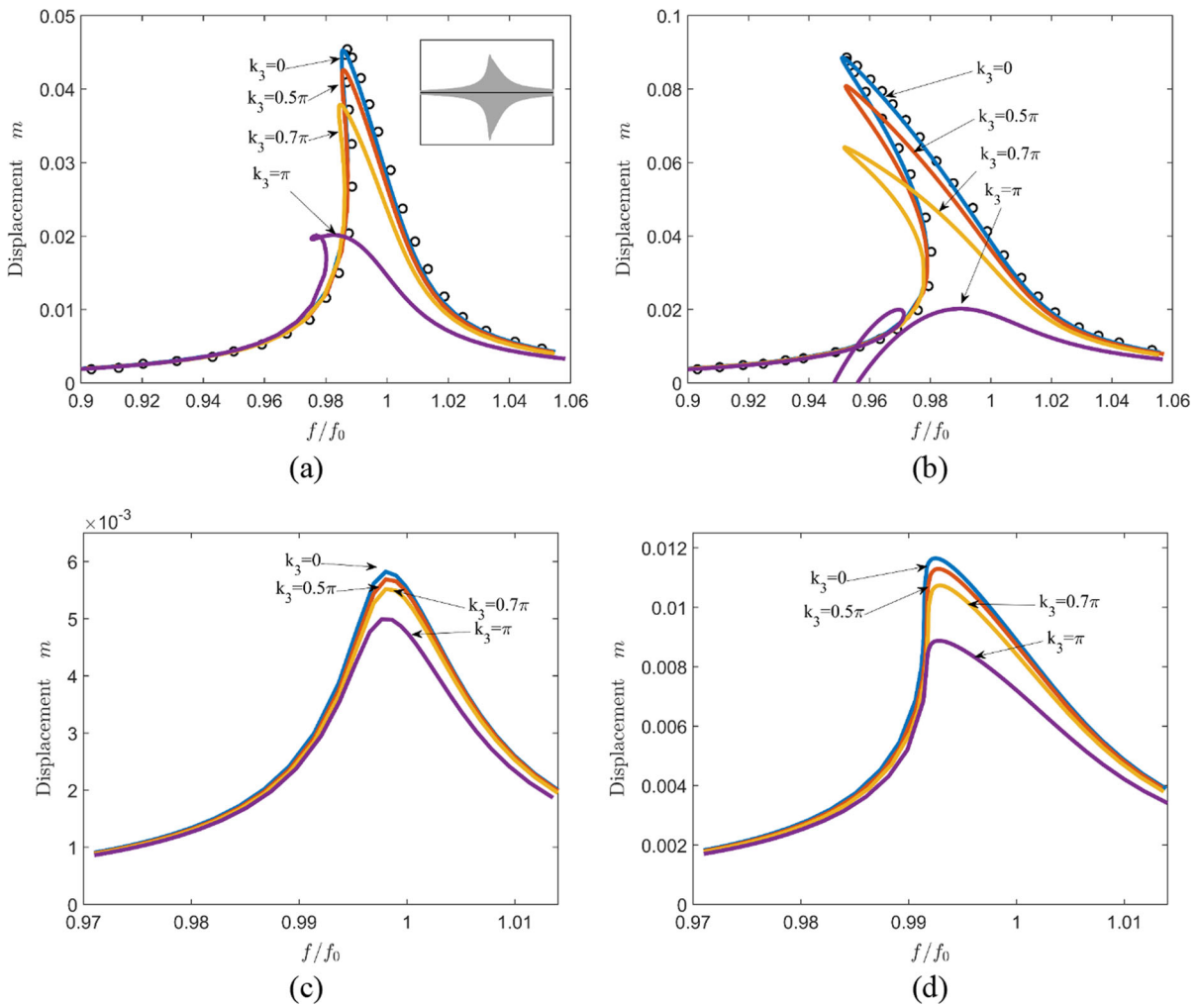

Fig. 9 NFR curves of higher modes with various initial curvatures and forcing levels. **a**, **b**: Mode 2 at the forcing level of 6 *N* and 12 *N*, respectively. **c**, **d**: Mode 3 at the forcing level of 6 *N* and 12 *N*, respectively. Circle in **a**, **b**: reference solution of the second mode for the straight beam

is reflected back to each harmonic. The energy level of the harmonics generally reduces when harmonic order increases. Note that the zero-order harmonic is the largest among all harmonic coefficients in Fig. 8d, e, since all even-order terms contribute to the zero-order coefficient through the quadratic order terms in the governing equation.

Considering the dominant nonlinear inertia, the straight cantilever beam essentially exhibits softening phenomenon in higher modes, which is different from the first mode [9]. Therefore, the curvature-induced effects on higher modes are demonstrated when the initial curvature is involved. To this end, the NFR curves of the second and third modes are depicted in Fig. 9 for different initial curvatures and forcing levels. With 6 N and 12 N excitation applied to the second mode, straight configuration shows good agreement between the results obtained from the HB continuation method and ROM (Fig. 9a, b). When the initial curvature is added, the resonance peaks of the curved beam shown in Fig. 9a reduce with the increasing initial curvature. To quantify the changes, the relative displacement ratio between the curved configurations $k_3 = 0$ and $k_3 = 0.7\pi$ is calculated, yielding 16.2%. The ratio increases up to 27.6% at the higher forcing level of 12 *N*, as shown in Fig. 9b. Meanwhile, the curved beams in higher modes show slight frequency shift when the initial curvature increases. Nevertheless, because of the curvature-induced quadratic terms in the governing equations, higher modes show asymmetric responses, which can be observed through time responses for the case of $k_3 = 0.7\pi$, shown in the subplot of Fig. 9a. This phenomenon becomes more obvious when the forcing level increases, as shown through comparisons between the two figures (Fig. 9a and b). Besides, with the largest initial curvature $k_3 = \pi$, Fig. 9a shows a loop in the second mode, which is further enlarged and heads down when the excitation force increases to 12 N, as depicted in Fig. 9b. The occurrence of negative displacement represents asymmetric vibration, which can be explained by Eq. (44). Similar patterns remain for the third mode (Fig. 9c and d). However, the third mode is more difficult to excite to trigger its inherent nonlinear behavior than the second mode, unless a larger excitation force is applied.

The initial curved deformation of the beam also depends on curved arclength l_c. Therefore, a longer arclength $l_c/L = 0.2$ is investigated. At a moderate forcing level of 1.5 N and 2 N, NFR curves in Fig. 10a show a reduction in the resonance frequency of the first mode. In this regard, increasing l_c leads to the same effects as k_3 in terms of hardening–softening transition in the first mode. However, at an even higher forcing level, 3 N, the NFR curve becomes more complex. In fact, four turning points can be observed, alongside a reversed trend, turning from softening to hardening. A plausible explanation can be offered. In a straight beam, the nonlinear stiffness dominates the first mode to produce the commonly observed

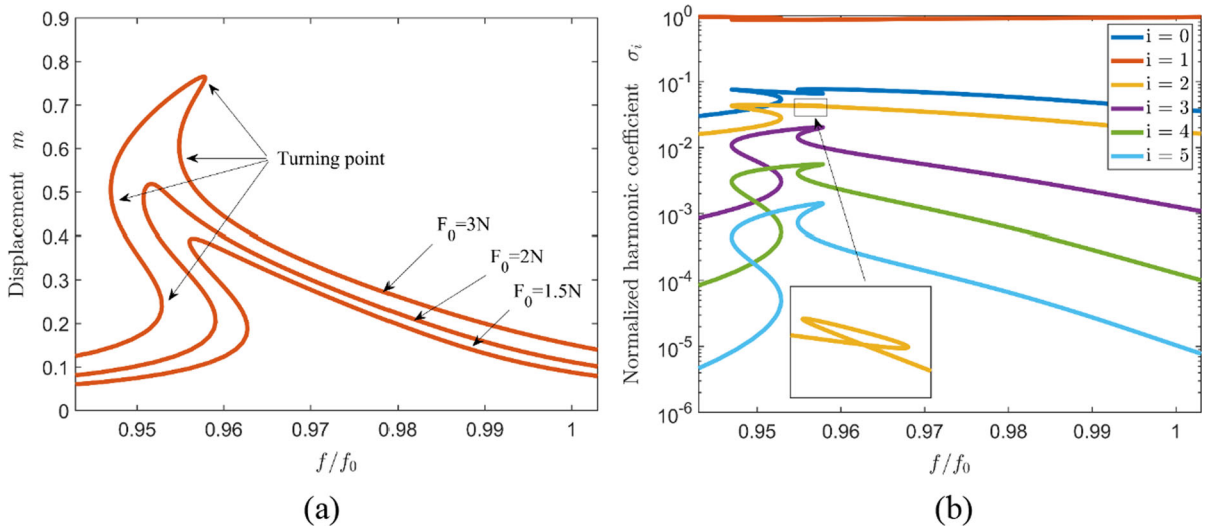

Fig. 10 **a** NFR curves for the first mode when $F_0 = [\,1.5N \quad 2N \quad 3N\,]$. **b** Normalized harmonic coefficients at the forcing level of 3 *N*

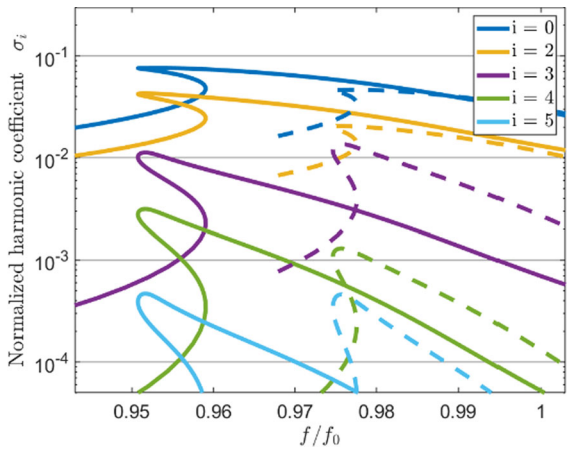

Fig. 11 Normalized harmonic coefficients of the first mode for different curved length at the forcing level of 2 *N*. Solid line:$l_c/L = 0.2$. Dashed line:$l_c/L = 0.1$

hardening phenomenon due to its large deformation. When the beam is initially curved, inertia effects are amplified and compete with the stiffness effects. However, for a sufficiently high forcing level, the larger deformation would enhance nonlinear stiffness effects to produce the ultimate softening-hardening behavior observed in Fig. 10a. Similar phenomenon is reflected in the normalized harmonic coefficients at the same forcing level of 3 N (Fig. 10b). In addition, the zero-order and the second harmonics show more complex variation, as evidenced by the appearance of loop, shown in the inset plots. It is relevant to note that nonlinear dynamic behaviors of the curved beam are not only determined by the curved condition (curvature and arclength), but also the excitation level.

To further substantiate the above, effects of different arclengths in terms of harmonics are compared. Figure 11 shows that the overall level of the normalized zero- and even-order harmonic coefficients increases with the curved arclength. However, variations of the odd-order coefficients are marginal and inconsistent in magnitude. For example, the third-order coefficient even decreases slightly. In general, an increase in the initial deformation of the beam would favor the generation of more energetic higher order harmonics, which at the same time generates increased energy transfer, mainly to the even-order components.

5 Conclusions

In this paper, a cantilever beam with constant initial curvature is investigated. Combining a geometrically exact model and the shortening effect, specific to a cantilever, an inextensible condensation model is established with the consideration of initial curvature. Specific techniques are proposed to numerically implement the developed model with increased accuracy and robustness. The proposed model explicitly shows different nonlinear stiffness and inertia terms arising from the initial curvature, as well as their interplay in the system equation. This explicit expression allows for the proposal of a modified Jacobian matrix calculation method (a necessity arising from the curvature-induced nonlinear inertia effects) involved in the HB method. Meanwhile, an OS technique is adopted and integrated into the generalized-α method for the calculation of time domain system responses.

The validity and the assumptions made for the development of the model are first validated through comparisons with COMSOL results based on linear FRFs and mode shape analyses. Results show that initial curvature and curved arclength both lead to a decrease in the resonance frequencies, more obvious when the beam is severely bent. Initial curvature causes increased longitudinal motion in the beam, which through its coupling with the transverse vibration, generates enhanced inertia effects. Numerical analyses demonstrate that both curvature-induced linear stiffness and inertia terms in the system equation are responsible for the reduction in the natural frequencies, which can be combined and regarded as effective inertia.

Confirmed by the time-domain results from the generalized-α method, nonlinear frequency responses of the first mode are shown to experience a hardening–softening transition with the increasing initial curvature. This is accompanied by a similar softening process in the harmonics. NFR curves become complex at a high forcing level which might create reversed trend from softening to hardening. The physical process behind can be explained. In fact, the initial curvature of the beam generates significant inertia effects which compete with the stiffness effects. With a sufficiently high forcing level, the stiffness effects eventually overwhelm and prevail to produce the observed softening-to-hardening

reversion. Higher modes, at an increased forcing level, show slight frequency downshifting while experiencing asymmetric responses. Both phenomena become more obvious when the forcing level increases.

As a final remark, this paper puts emphasis on some fundamental issues related to the intrinsic nonlinearities and inertia-induced features in an initially deformed cantilever from the perspective of system modeling and analyses. The model could be refined and further developed for other structural configurations.

Acknowledgements Authors thank the Research Grant Council of the Hong Kong SAR (PolyU 152023/20E) for financial support.

Funding The authors have not additional funding.

Data availability The datasets generated during and/or analyzed during the current study are available from the corresponding author on reasonable request.

Declarations

Conflict of interest The authors declare that they have no conflict of interest.

Appendix 1

The generalized-α method

The generalized-α method is applied to offer intuitive time history of the system responses. In the main text, Eq. (19) requires the treatment of different system response terms, especially displacement $\mathbf{x}$, as well as its derivatives representing velocity $\dot{\mathbf{x}}$ and acceleration $\ddot{\mathbf{x}}$. The interrelation among them can be cast into the following general form [54]:

$$\begin{aligned}\dot{\mathbf{x}}_{i+1} &= \dot{\mathbf{x}}_i + (1-\gamma)\Delta t\ddot{\mathbf{x}}_i + \gamma\Delta t\ddot{\mathbf{x}}_{i+1}\\ \mathbf{x}_{i+1} &= \mathbf{x}_i + \Delta t\dot{\mathbf{x}}_i + \Delta t^2\left(\frac{1}{2}-\beta\right)\ddot{\mathbf{x}}_i + \Delta t^2\beta\ddot{\mathbf{x}}_{i+1}\end{aligned} \tag{46}$$

The governing equation of motion, Eq. (19), is built on semi-point scheme in the time discretization. The semi-point values of these quantities write

$$\begin{aligned}\mathbf{x}_{i+1-\alpha_f} &= (1-\alpha_f)\mathbf{x}_{i+1} + \alpha_f\mathbf{x}_i\\ \dot{\mathbf{x}}_{i+1-\alpha_f} &= (1-\alpha_f)\dot{\mathbf{x}}_{i+1} + \alpha_f\dot{\mathbf{x}}_i\\ \ddot{\mathbf{x}}_{i+1-\alpha_m} &= (1-\alpha_m)\ddot{\mathbf{x}}_{i+1} + \alpha_m\ddot{\mathbf{x}}_i\\ t_{i+1-\alpha_f} &= (1-\alpha_f)t_{i+1} + \alpha_f t_i\end{aligned} \tag{47}$$

A residual vector is formulated from Eq. (19) as

$$\mathbf{r}(\mathbf{x}) = \mathbf{M}\ddot{\mathbf{x}} + C\dot{\mathbf{x}} + \mathbf{K}\mathbf{x} + \mathbf{f}_{nl}(\mathbf{x},\dot{\mathbf{x}},\ddot{\mathbf{x}}) - \mathbf{f}_{ext} = \mathbf{0} \tag{48}$$

Discretized version of the above equation in terms of $(\mathbf{x}_{i+1-\alpha_f}, \dot{\mathbf{x}}_{i+1-\alpha_f}, \ddot{\mathbf{x}}_{i+1-\alpha_m})$ writes

$$\mathbf{r}\left(\mathbf{x}_{i+1-\alpha_f}, \dot{\mathbf{x}}_{i+1-\alpha_f}, \ddot{\mathbf{x}}_{i+1-\alpha_m}\right) = \mathbf{0} \tag{49}$$

Let us denote $(\mathbf{x}^k_{i+1-\alpha_f}, \dot{\mathbf{x}}^k_{i+1-\alpha_f}, \ddot{\mathbf{x}}^k_{i+1-\alpha_m})$ as the approximate value of $(\mathbf{x}_{i+1-\alpha_f}, \dot{\mathbf{x}}_{i+1-\alpha_f}, \ddot{\mathbf{x}}_{i+1-\alpha_m})$ resulting from the iteration k. In the vicinity of the prediction value, the residual equation can be replaced with sufficient accuracy through the following linear expression:

$$\mathbf{r}^{k+1} \approx \mathbf{r}^k + \mathbf{S}^k\Delta\mathbf{x}^k_{i+1-\alpha_f} = \mathbf{r}^k + \mathbf{S}^k_T\Delta\mathbf{x}^k_{i+1} = \mathbf{0} \tag{50}$$

in which the Jacobian (also called iteration) matrix writes:

$$\mathbf{S}^k_T = (1-\alpha_f)\left.\frac{\partial\mathbf{r}}{\partial\mathbf{x}}\right|_{\mathbf{x}^k_{i+1-\alpha_f}} \tag{51}$$

whose expression is detailed as

$$\begin{aligned}\mathbf{S}_T(\mathbf{x}) = (1-\alpha_f)&\\ \left(\mathbf{M}\frac{\partial\ddot{\mathbf{x}}}{\partial\mathbf{x}} + \mathbf{C}\frac{\partial\dot{\mathbf{x}}}{\partial\mathbf{x}} + \mathbf{K} + \frac{\partial\mathbf{f}_{nl}}{\partial\mathbf{x}} + \frac{\partial\mathbf{f}_{nl}}{\partial\dot{\mathbf{x}}}\frac{\partial\dot{\mathbf{x}}}{\partial\mathbf{x}} + \frac{\partial\mathbf{f}_{nl}}{\partial\ddot{\mathbf{x}}}\frac{\partial\ddot{\mathbf{x}}}{\partial\mathbf{x}}\right)\end{aligned} \tag{52}$$

The integration relationship, Eq.(46), can be written as

$$\frac{\partial\ddot{\mathbf{x}}_{i+1-\alpha_m}}{\partial\mathbf{x}_{i+1-\alpha_f}} = \frac{1-\alpha_m}{(1-\alpha_f)\beta\Delta t^2}\mathbf{I}, \quad \frac{\partial\dot{\mathbf{x}}_{i+1-\alpha_f}}{\partial\mathbf{x}_{i+1-\alpha_f}} = \frac{\gamma}{\beta\Delta t}\mathbf{I} \tag{53}$$

Combining Eqs. (52) and (53) yields the expression of the iteration matrix as:

$$\begin{aligned}\mathbf{S}_T(\mathbf{x}) = \frac{1-\alpha_m}{\beta\Delta t^2}\mathbf{M} + \frac{\gamma(1-\alpha_f)}{\beta\Delta t}\mathbf{C} + (1-\alpha_f)\mathbf{K}&\\ +(1-\alpha_f)\frac{\partial\mathbf{f}_{nl}}{\partial\mathbf{x}} + \frac{\gamma(1-\alpha_f)}{\beta\Delta t}\frac{\partial\mathbf{f}_{nl}}{\partial\dot{\mathbf{x}}} + \frac{1-\alpha_m}{\beta\Delta t^2}\frac{\partial\mathbf{f}_{nl}}{\partial\ddot{\mathbf{x}}}&\end{aligned} \tag{54}$$

The nonlinear equation (50) is then solved using an iteration scheme using Newton–Raphson method. Substituting Eqs. (46 and 47) into Eq. (50) gives

$$\mathbf{S}_T^k \Delta \mathbf{x}_{i+1}^k = -\mathbf{r}^k \tag{55}$$

with

$$\begin{aligned}
\mathbf{r}^k &= \beta \Delta t^2 \mathbf{S}_L \ddot{\mathbf{x}}_{i+1}^k + \mathbf{f}_{nl,i+1}^k - \mathbf{p}_{i+1} \\
\mathbf{S}_L &= \frac{1-\alpha_m}{\beta \Delta t^2}\mathbf{M} + \frac{\gamma(1-\alpha_f)}{\beta \Delta t}\mathbf{C} + (1-\alpha_f)\mathbf{K} \\
\mathbf{p}_{i+1} &= (1-\alpha_f)\mathbf{f}_{ext,i+1} + \alpha_f \mathbf{f}_{ext,i} - (\mathbf{a}_1 \mathbf{x}_i + \mathbf{a}_2 \dot{\mathbf{x}}_i + \mathbf{a}_3 \ddot{\mathbf{x}}_i) \\
\mathbf{a}_1 &= \mathbf{K} \\
\mathbf{a}_2 &= \mathbf{C} + (1-\alpha_f)\Delta t \mathbf{K} \\
\mathbf{a}_3 &= \alpha_m \mathbf{M} + (1-\alpha_f)(1-\gamma)\Delta t \mathbf{C} + \Delta t^2 (1-\alpha_f)\left(\frac{1}{2} - \beta\right)\mathbf{K}
\end{aligned} \tag{56}$$

The velocity and acceleration are found from

$$\Delta \ddot{\mathbf{x}}_{i+1}^k = \frac{1}{\beta \Delta t^2}\Delta \mathbf{x}_{i+1}^k, \quad \Delta \dot{\mathbf{x}}_{i+1}^k = \frac{\gamma}{\beta \Delta t}\Delta \mathbf{x}_{i+1}^k \tag{57}$$

When $k = 0$, the initial prediction to initialize the process is $\ddot{\mathbf{x}}_{i+1}^0 = \ddot{\mathbf{x}}_i$ as the first-order approximation, which would need more correction steps.

To simplify the process and reduce the computation burden, an alternative prediction formulation with third-order precision, i.e.,$\ddot{\mathbf{x}}_{i+1}^0 = 4\ddot{\mathbf{x}}_i - 6\ddot{\mathbf{x}}_{i-1} + 4\ddot{\mathbf{x}}_{i-2} - \ddot{\mathbf{x}}_{i-3}$, is proposed by using the four latest points. Stepwise correction continues until $||\mathbf{r}(\mathbf{x}_{i+1}^k)|| \leq \varepsilon$, where ε is a predefined tolerance value.

The above calculation scheme is combined with the generalized-α method [54]. The parameters are chosen as follows

$$\begin{aligned}
\alpha_m &= \frac{2\rho_\infty - 1}{\rho_\infty + 1}, \quad \alpha_f = \frac{\rho_\infty}{\rho_\infty + 1}, \quad \rho_\infty \in [0,\ 1] \\
\gamma &= \frac{1}{2} - \alpha_m + \alpha_f, \quad \beta = \frac{1}{4}(1 - \alpha_m + \alpha_f)^2
\end{aligned} \tag{58}$$

The dissipation parameter ρ_∞ is set to 0.8 in the present study.

Appendix 2

Efficiency and robustness enhanced by OS technique

The OS technique discussed in Sect. 3.2 is expected to improve the efficiency and the robustness of the generalized-α method by separating a full complex problem into several sub-problems. To demonstrate this, the generalized-α methods with and without the OS technique are compared using a beam vibration problem.

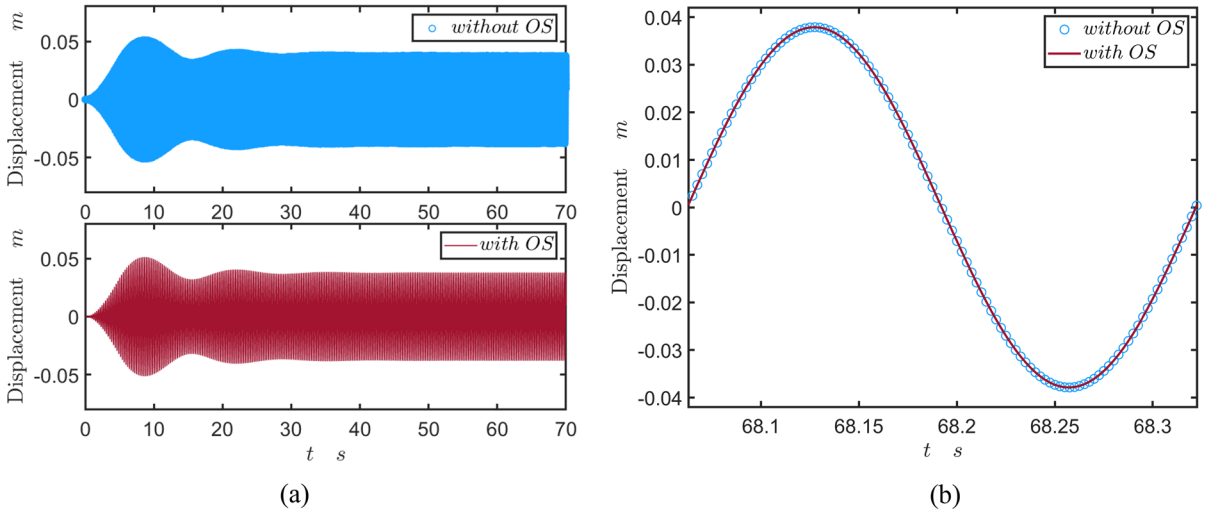

(a) (b)

Fig. 12 **a** Time responses obtained by the generalized-α method with and without OS technique, **b** close-up view taken in the stable region for a period. Note the two curves coincide perfectly, so it is difficult to visually differentiate them

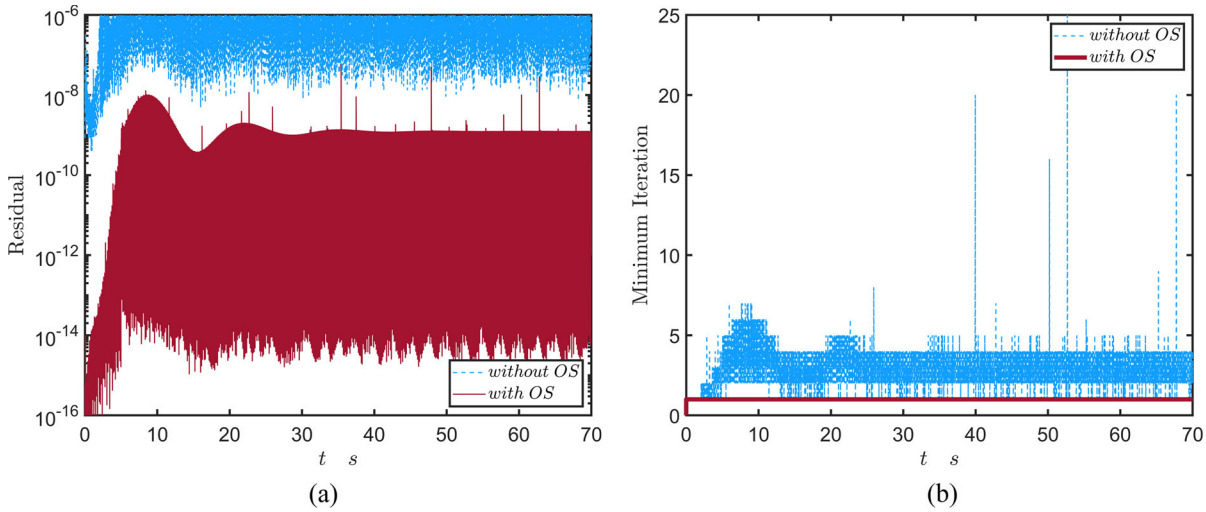

Fig. 13 **a** Residual and **b** minimum iteration in each time point obtained by the generalized-α method with and without OS technique. Note in Figure 13 **b**, the method using OS needs only one iteration to reach the convergence

Examine the straight cantilever beam (used in Sect. 4) excited by a harmonic force at its free end. The excitation force has an amplitude 0.5 N at 3.85 Hz, which is arbitrarily chosen around the first natural frequency of the beam. The computation duration is 70 s, which is long enough to get stable response in the system. The sampling frequency is $f_s = 400$ Hz. Figure 12a illustrates the overall time response signals obtained by using the two methods. The two curves coincide completely during the entire time duration, as better shown in the close-up view (Fig. 12b). The residual values (as defined by Eq. (56) in Appendix 1) are calculated for both methods and shown in Fig. 13a. It follows that OS technique yields very small residuals, which are smaller than the ones without OS for nearly every single time point, demonstrating the accuracy of the proposed OS technique. Figure 13b shows the minimum iteration number required to achieve converged result with a residual value capped at 10^{-6}. It can be seen that, by embedding the OS technique into the generalized-α method, it takes only one iteration to reach converged result, while more iterations are required without OS technique. This happens even within the stable region. Moreover, it was also noticed that generalized-α method without OS technique may not always yield converged solution for some frequencies, while the one with OS technique always does. The above comparison shows the high efficiency and the robustness of the generalized-α method after embedding the proposed OS technique.

References

1. Pai, P.F., Nayfeh, A.H.: A fully nonlinear theory of curved and twisted composite rotor blades accounting for warpings and three-dimensional stress effects. Int. J. Solids Struct. **31**(9), 1309–1340 (1994)
2. Nayfeh, A.H., Lacarbonara, W., Chin, C.-M.: Nonlinear normal modes of buckled beams: three-to-one and one-to-one internal resonances. Nonlinear Dyn. **18**(3), 253–273 (1999)
3. Yu, A.M., Yang, J.W., Nie, G.H., Yang, X.G.: An improved model for naturally curved and twisted composite beams with closed thin-walled sections. Compos. Struct. **93**(9), 2322–2329 (2011)
4. Ghayesh, M.H., Amabili, M.: Coupled longitudinal-transverse behaviour of a geometrically imperfect microbeam. Compos. B Eng. **60**, 371–377 (2014)
5. Yi, Z., Stanciulescu, I.: Nonlinear normal modes of a shallow arch with elastic constraints for two-to-one internal resonances. Nonlinear Dyn. **83**(3), 1577–1600 (2016)
6. Qiao, W., Guo, T., Kang, H., Zhao, Y.: Softening–hardening transition in nonlinear structures with an initial curvature: a refined asymptotic analysis. Nonlinear Dyn. **107**(1), 357–374 (2022)
7. Touzé, C., Vizzaccaro, A., Thomas, O.: Model order reduction methods for geometrically nonlinear structures: a review of nonlinear techniques. Nonlinear Dyn. **105**(2), 1141–1190 (2021)
8. Lacarbonara, W.: Nonlinear structural mechanics: theory, dynamical phenomena and modeling. Springer (2013)

9. Nayfeh, A.H., Pai, P.F.: Linear and nonlinear structural mechanics. Wiley (2008)
10. Ding, H., Chen, L.-Q.: Nonlinear vibration of a slightly curved beam with quasi-zero-stiffness isolators. Nonlinear Dyn. **95**(3), 2367–2382 (2019)
11. Kármán, T.V.: Festigkeitsprobleme im Maschinenbau. In: Klein, F., Müller, C. (eds.) Mechanik, pp. 311–385. Vieweg+Teubner Verlag, Wiesbaden (1907)
12. Lagnese, J.E.: Boundary stabilization of thin plates. SIAM (1989)
13. Lagnese, J.E., Leugering, G.: Uniform stabilization of a nonlinear beam by nonlinear boundary feedback. J. Differ. Equ. **91**(2), 355–388 (1991)
14. Koch, H., Lasiecka, I.: Hadamard Well-posedness of Weak Solutions in Nonlinear Dynamic Elasticity-full von Karman Systems. In: Lorenzi, A., Ruf, B. (eds.) Evolution Equations, pp. 197–216. Semigroups and Functional Analysis. In Memory of Brunello Terreni, Birkhäuser Basel, Basel (2002)
15. Alijani, F., Amabili, M.: Non-linear vibrations of shells: A literature review from, 2003 to 2013. Int. J. Non-Linear Mech. **58**, 233–257 (2014)
16. Nayfeh, A.H., Mook, D.T.: Nonlinear oscillations. Wiley, UK (2008)
17. Amabili, M.: Nonlinear vibrations and stability of shells and plates. Cambridge University Press (2008)
18. Bhashyam, G.R., Prathap, G.: Galerkin finite element method for non-linear beam vibrations. J. Sound Vib. **72**(2), 191–203 (1980)
19. Lee, J., Kerschen, G., Detroux, T.: Harmonic balance computation of the nonlinear frequency response of a thin plate, (2017)
20. Amabili, M.: Theory and experiments for large-amplitude vibrations of rectangular plates with geometric imperfections. J. Sound Vib. **291**(3), 539–565 (2006)
21. Touzé, C., Camier, C., Favraud, G., Thomas, O.: Effect of imperfections and damping on the type of nonlinearity of circular plates and shallow spherical shells. Math. Probl. Eng. **2008**, 678307 (2008)
22. Lacarbonara, W., Arafat, H.N., Nayfeh, A.H.: Non-linear interactions in imperfect beams at veering. Int. J. Non-Linear Mech. **40**(7), 987–1003 (2005)
23. Yi, Z., Wang, L., Kang, H., Tu, G.: Modal interaction activations and nonlinear dynamic response of shallow arch with both ends vertically elastically constrained for two-to-one internal resonance. J. Sound Vib. **333**(21), 5511–5524 (2014)
24. Bauchau, O.A., Hong, C.H.: Large displacement analysis of naturally curved and twisted composite beams. AIAA J. **25**(11), 1469–1475 (1987)
25. Ibrahimbegović, A.: On finite element implementation of geometrically nonlinear Reissner's beam theory: three-dimensional curved beam elements. Comput. Methods Appl. Mech. Eng. **122**(1), 11–26 (1995)
26. Crespo da Silva, M.R.M., Glynn, C.C.: Nonlinear flexural-flexural-torsional dynamics of inextensional beams. I. Equations of motion. J. Struct. Mech. **6**(4), 437–448 (1978)
27. Culver, D., McHugh, K., Dowell, E.: An assessment and extension of geometrically nonlinear beam theories. Mech. Syst. Signal Process. **134**, 106340 (2019)
28. Nayfeh, A.H., Pai, P.F.: Non-linear non-planar parametric responses of an inextensional beam. Int. J. Non-Linear Mech. **24**(2), 139–158 (1989)
29. Thomas, O., Sénéchal, A., Deü, J.F.: Hardening/softening behavior and reduced order modeling of nonlinear vibrations of rotating cantilever beams. Nonlinear Dyn. **86**(2), 1293–1318 (2016)
30. McHugh, K., Dowell, E.: Nonlinear responses of inextensible cantilever and free-free beams undergoing large deflections. J. Appl. Mech. **85**(5), 051008 (2018)
31. Dowell, E., McHugh, K.: Equations of motion for an inextensible beam undergoing large deflections. J. Appl. Mech. (2016). https://doi.org/10.1115/1.4032795
32. Anderson, T.J., Nayfeh, A.H., Balachandran, B.: Experimental verification of the importance of the nonlinear curvature in the response of a cantilever beam. J. Vib. Acoust. **118**(1), 21–27 (1996)
33. Kumar, A.: Effect of approximation of curvature/inertia on the nonlinear vibrations of cantilever beam. Structures **26**, 737–744 (2020)
34. Farokhi, H., Xia, Y., Erturk, A.: Experimentally validated geometrically exact model for extreme nonlinear motions of cantilevers. Nonlinear Dyn. **107**(1), 457–475 (2022)
35. Amabili, M., Ferrari, G., Ghayesh, M.H., Hameury, C., Hena Zamal, H.: Nonlinear vibrations and viscoelasticity of a self-healing composite cantilever beam: Theory and experiments. Compos. Struct. **294**, 115741 (2022)
36. Semler, C., Li, G.X., Païdoussis, M.P.: The non-linear equations of motion of pipes conveying fluid. J. Sound Vib. **169**(5), 577–599 (1994)
37. Paidoussis, M.P.: Fluid-structure interactions: slender structures and axial flow. Academic press (1998)
38. Deliyianni, M., McHugh, K., Webster, J.T., Dowell, E.: Dynamic equations of motion for inextensible beams and plates. Arch. Appl. Mech. **92**(6), 1929–1952 (2022)
39. McHugh, K.A., Dowell, E.H.: Nonlinear response of an inextensible, cantilevered beam subjected to a nonconservative follower force. J. Comput. Nonlinear Dyn. **14**(3), (2019)
40. Malatkar, P.: Nonlinear vibrations of cantilever beams and plates. Virginia Polytechnic Institute and State University (2003)
41. Deliyianni, M., Webster, J.T.: Theory of solutions for an inextensible cantilever. Appl. Math. Optim. **84**(2), 1345–1399 (2021)
42. Deliyianni, M., Gudibanda, V., Howell, J., Webster, J.T.: Large deflections of inextensible cantilevers: modeling, theory, and simulation. Math. Model. Nat. Phenom. **15**, 44 (2020)
43. Amabili, M., Paıdoussis, M.P.: Review of studies on geometrically nonlinear vibrations and dynamics of circular cylindrical shells and panels, with and without fluid-structure interaction. Appl. Mech. Rev. **56**(4), 349–381 (2003)
44. Pan, K.-Q., Liu, J.-Y.: Geometric nonlinear dynamic analysis of curved beams using curved beam element. Acta. Mech. Sin. **27**(6), 1023–1033 (2011)
45. Liu, J., Hong, J., Cui, L.: An exact nonlinear hybrid-coordinate formulation for flexible multibody systems. Acta. Mech. Sin. **23**(6), 699–706 (2007)

46. Tang, S., Sweetman, B.: A geometrically-exact momentum-based non-linear theory applicable to beams in non-inertial frames. Int. J. Non-Linear Mech. **113**, 158–170 (2019)
47. Zulli, D., Alaggio, R., Benedettini, F.: Non-linear dynamics of curved beams Part 1: formulation. Int. J. Non-Linear Mech. **44**(6), 623–629 (2009)
48. Zulli, D., Alaggio, R., Benedettini, F.: Non-linear dynamics of curved beams. Part 2, numerical analysis and experiments. Int. J. Non-Linear Mech. **44**(6), 630–643 (2009)
49. Shen, Y., Vizzaccaro, A., Kesmia, N., Yu, T., Salles, L., Thomas, O., Touzé, C.: Comparison of reduction methods for finite element geometrically nonlinear beam structures. Vibration **4**(1), 175–204 (2021)
50. Cochelin, B., Vergez, C.: A high order purely frequency-based harmonic balance formulation for continuation of periodic solutions. J. Sound Vib. **324**(1), 243–262 (2009)
51. Woiwode, L., Balaji, N.N., Kappauf, J., Tubita, F., Guillot, L., Vergez, C., Cochelin, B., Grolet, A., Krack, M.: Comparison of two algorithms for harmonic balance and path continuation. Mech. Syst. Signal Process. **136**, 106503 (2020)
52. Detroux, T., Renson, L., Masset, L., Kerschen, G.: The harmonic balance method for bifurcation analysis of large-scale nonlinear mechanical systems. Comput. Methods Appl. Mech. Eng. **296**, 18–38 (2015)
53. Detroux, T., Noël, J.-P., Virgin, L.N., Kerschen, G.: Experimental study of isolas in nonlinear systems featuring modal interactions. PLoS ONE **13**(3), e0194452 (2018)
54. Chung, J., Hulbert, G.M.: A time integration algorithm for structural dynamics with improved numerical dissipation: the generalized-α method. J. Appl. Mech. **60**(2), 371–375 (1993). https://doi.org/10.1115/1.2900803
55. Pai, P.F., Anderson, T.J., Wheater, E.A.: Large-deformation tests and total-Lagrangian finite-element analyses of flexible beams. Int. J. Solids Struct. **37**(21), 2951–2980 (2000)
56. Pai, P.F.: Problems in geometrically exact modeling of highly flexible beams. Thin-Walled Struct. **76**, 65–76 (2014)
57. Webb, J.: Imposing linear constraints in finite-element analysis. Commun. Appl. Numer. Methods **6**(6), 471–475 (1990)
58. Cameron, T.M., Griffin, J.H.: An alternating frequency/time domain method for calculating the steady-state response of nonlinear dynamic systems. J. Appl. Mech. **56**(1), 149–154 (1989)
59. Tang, D., Zhao, M., Dowell, E.H.: Inextensible beam and plate theory: computational analysis and comparison with experiment. J. Appl. Mech. (2014). https://doi.org/10.1115/1.4026800
60. Peeters, M., Viguié, R., Sérandour, G., Kerschen, G., Golinval, J.C.: Nonlinear normal modes, Part II: toward a practical computation using numerical continuation techniques. Mech. Syst. Signal Process. **23**(1), 195–216 (2009)
61. Coddington, E.A., Levinson, N.: Theory of ordinary differential equations. Tata McGraw-Hill Education (1955)